Flight Dynamics of Boomerangs: Impact of Reversal of Airflow, Reversal of Angle-of-Attack and Asymmetric Lift

Prasad S. Gudem,[1]
University of California at San Diego, La Jolla, California 92093, USA

Manuel Schütz,[2]
WKS KV Bern, Bern 3001, Switzerland

and
Kyle Holland[3]
Qualcomm Technologies Incorporated, San Diego, California 92121, USA

Translation velocity combined with rotational velocity results in blade segments of a boomerang experiencing reversal of airflow and reversal of angle-of-attack as they traverse the 360^0 angles of rotation. In this paper, we extent prior work by including the impact of reversal of airflow and reversal of angle-of-attack in deriving expressions for lift and rolling-moment. In addition, we derived an expression for pitching-moment considering the location of lift is asymmetric with respect to axis of symmetry of the blade of a boomerang *and* switches polarity across the axis of symmetry of the boomerang blade due to reversal of airflow. Contrary to the conclusions in earlier work, our analysis shows that pitching-moment is not zero. This is important, as pitching-moment is essential to explain nutation (layover) during a boomerang flight. We combined the expressions derived for lift, rolling-moment and pitching-moment to numerically simulate the trajectory of a boomerang in level flight; including the pitching-moment results in nutation and an elliptical flight path. These results are consistent with the observed flight behavior of boomerangs. Finally, it is noted that the theory developed here is also applicable to lightweight fast-moving drones where the blade segments experience reversal of airflow and reversal of angle-of-attack.

[1] Adjunct Associate Professor, Department of Electrical and Computer Engineering.
[2] Grammar School Teacher in Physics and Mathematics.
[3] Staff Engineer, Radio Frequency Integrated Circuits Group.

Nomenclature

C = Chord length (m)

C_{l0+} = 2D lift coefficient for leading edge at α = 0

C_{l0-} = 2D lift coefficient for trailing edge at α = 0

$C_{l\alpha+}$ = 2D lift-curve slope for leading edge (per rad)

$C_{l\alpha-}$ = 2D lift-curve slope for trailing edge (per rad)

$\overline{C_{L0}}$ = 2D non-dimensional lift coefficient at α = 0

$\overline{C_{L\alpha}}$ = 2D non-dimensional lift-curve slope (per rad)

$\overline{C_{MX0}}$ = Basic non-dimensional rolling-moment (N.m)

$\overline{C_{MX\alpha}}$ = Non-dimensional rolling-moment due to angle-of-attack (N.m)

$\overline{C_{MY0}}$ = Basic non-dimensional Pitching-moment (N.m)

$\overline{C_{MY\alpha}}$ = Non-dimensional Pitching-moment due to angle-of-attack (N.m)

g = Gravitational acceleration (9.8 m/sec^2)

I_X = Moment of inertia in the X-axis (N.m)

I_Y = Moment of inertia in the Y-axis (N.m)

I_Z = Moment of inertia in the Z-axis (N.m)

L = Lift (N)

L_0 = Basic lift (N)

L_0^+ = Basic lift for leading edge (N)

L_0^- = Basic lift for trailing edge (N)

L_α = Lift due to angle-of-attack (N)

L_α^+ = Lift due to angle-of-attack for leading edge (N)

L_α^- = Lift due to angle-of-attack for trailing edge (N)

m = Mass of the boomerang

M_X = Rolling-moment (N.m)

M_{X0} = Basic Rolling-moment (N.m)

M_{X0}^+ = Basic rolling-moment for leading edge (N.m)

M_{X0}^- = Basic rolling-moment for trailing edge (N.m)

$M_{X\alpha}$ = Rolling-moment due to angle-of-attack (N.m)

$M_{X\alpha}^{+}$ = Rolling-moment due to angle-of-attack for leading edge (N.m)

$M_{X\alpha}^{-}$ = Rolling-moment due to angle-of-attack for trailing edge (N.m)

M_{Y} = Pitching-moment (N.m)

M_{Y0} = Basic Pitching-moment (N.m)

M_{Y0}^{+} = Pitching-moment for leading edge (N.m)

M_{Y0}^{-} = Pitching-moment for trailing edge (N.m)

$M_{Y\alpha}$ = Pitching-moment due to angle-of-attack (N.m)

$M_{Y\alpha}^{+}$ = Pitching-moment for leading edge due to angle-of-attack (N.m)

$M_{Y\alpha}^{-}$ = Pitching-moment for trailing edge due to angle-of-attack (N.m)

r = Radial coordinate (m)

R = Blade length (m)

R_{offset} = Offset for lift from axis of symmetry of the blade (m)

V = Translational velocity of the boomerang (m/s)

V_n = Velocity normal (perpendicular) to the wind (m/s)

α = Angle-of-attack (rad)

θ = Euler angle between z-axis and Z-axis (rad)

ϕ = Euler angle between x-axis and N-axis (rad)

ψ = Euler angle between N-axis and X-axis (rad)

ρ = Air density (kg/m^3)

χ = Non-dimensional rotational velocity of blade tip $\left(\frac{R\omega}{V}\right)$

ω = Rotational velocity (rad/s)

I. Introduction

The boomerang is a simple and ingenious device invented by man thousands of years ago. Primitive societies used rocks and sticks to hunt animals. They probably discovered by accident that a stick bent at the center (also called throwing sticks, non-returning boomerangs or Kylies) traveled farther with better accuracy than a straight stick providing a strategic advantage in hunting prey. The returning boomerang was likely invented from the non-returning boomerang by accident and further refined through trial and error. Although non-returning boomerangs were unearthed in many parts of the world, remarkably, only the aboriginals in Australia invented the returning boomerangs. Most boomerangs are thrown almost at a vertical orientation to the ground at a slight upward elevation to the horizon and return to the thrower at a horizontal (flat) orientation to the ground.

Many modifications to the traditional V-shaped boomerang have been explored over the many centuries since their invention by Australian aboriginals. More recently, boomerang championships have been gaining popularity in many countries. The international federation of boomerang associations developed the rules for the various individual and team events (Accuracy, Fast Catch, Aussie Round, Long Distance, MTA, etc.) [1]. These competitions have driven the boomerang sports enthusiasts to modify the traditional Australian V-shaped boomerangs to better meet the needs of the specific competitive events [2] (see Fig. 1). For example, boomerangs with three wings (also called three-bladers) are almost universally used in the fast catch event where the goal is to throw and catch the boomerang five consecutive times in the shortest possible time while reaching at least 20m for each throw. The current world record for fast catch is 14.07 seconds, held by Manuel Schütz. Similarly, two-wing, V-shaped boomerangs are almost exclusively used in the Australian round where the goal is to throw the boomerang 50m and catch it in the bullseye for maximum points. The current world record is 99 points, held by Fridolin Frost. Yet another event is the long-distance (LD) event, where the goal is to throw the boomerang as far as possible and return past the finish line. LD boomerangs are shaped like a hook and unlike other boomerangs are thrown almost flat (horizontal orientation). The current world record is 238m, set by Manuel Schütz in 1999. In maximum time aloft (MTA), the goal is to keep the boomerang in the air for as long as possible. Boomerangs with wings swept forward are frequently used in this event. The current world record is 380.59 seconds, set by Billy Brazelton in 2010. More details on boomerang championship world records can be found in [3].

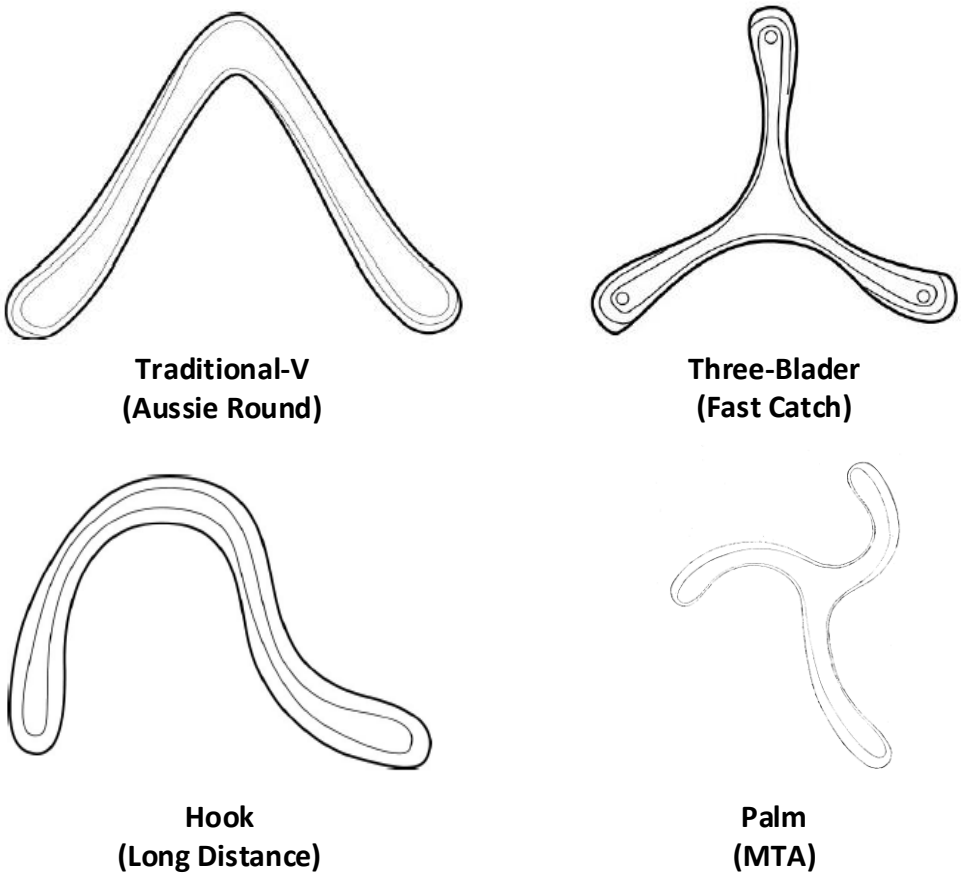

Fig. 1: Sample of boomerangs used in competitive championships (courtesy of [2]).

Despite the simplicity of the device, the flight dynamics of a boomerang is rather complex. Boomerang designs are often developed using rules of thumb developed through numerous iterations of trial and error combined with a basic understanding of aerodynamics of boomerangs [4, 5]. In the 1970s, Felix Hess developed the aerodynamic equations to numerically simulate the flight trajectory of a boomerang [6]. He collected a large amount of experimental data for various geometrical shapes and initial conditions and compared them with numerical simulation results. Based on this extensive study, he developed a simple model for a circular flight path of a boomerang, often referred to as Hess's model. In 2004, Azuma Beppu carried out an in-depth study of the flight dynamics of boomerangs with different boomerang joint wing angles and for various initial launch conditions using numerical techniques [7, 8]. In 2012, Vassberg took a significant step forward by deriving analytical expressions to study the flight dynamics of a boomerang using blade element theory [9]. Closed-form expressions for basic and angle-of-attack (AOA) lift and

rolling-moment were derived and the results were used to derive an elegant expression for the radius of the circular flight path.

The goal of this research is to enhance the existing knowledge on the flight dynamics of boomerangs. The theory developed here is also applicable to lightweight fast-moving drones that are recently gaining popularity due to rapid growth in wireless technology used in the guidance, navigation and control. This paper is organized as follows. In section II, we study the lift coefficients of a typical boomerang airfoil for leading edge and trailing edge for positive and negative angle-of-attack. In section III, we derive expressions for time-averaged lift and rolling-moment while separately accounting for lift and rolling-moment for leading edge versus trailing edge. In section IV, we derive an expression for pitching-moment considering lift is generated at an offset from axis of symmetry of the blade and switches polarity when the airflow reverses from leading edge to trailing edge. In addition, the complex expressions in section IV, are greatly simplified to develop compact expressions that can be readily used with minimal loss of accuracy for practical range of non-dimensional angular speeds. In section V, we simulate the flight trajectory of a boomerang using the expressions derived in sections III & IV. Our simulation results adequately describe the key features of a boomerang flight – nutation (layover) and elliptical trajectory. Section VI provides the summary and conclusions.

Table 1: Typical Boomerangs Flight Parameters.

Typical Range of Boomerang Properties			
	Min.	Typ.	Max.
Radius (Effective)	5cm	15cm	30cm
Blade Width	1cm	4cm	10cm
Blade Thickness	0.5mm	2mm	10mm
Blade Pitch	0deg	5deg	10deg
Mass	3g	50g	150g

Typical Range of Operating Conditions of a Boomerang			
	Min.	Typ.	Max.
Initial Translational Speed	10m/s	20m/s	35m/s
Final Translational Speed	0m/s	10m/s	20m/s
Initial Rotational Speed	5Hz	10Hz	25Hz
Final Rotational Speed	0Hz	5Hz	15Hz
Initial Launch Angle	45deg	75deg	90deg
Final Return Angle	0deg	20deg	50deg

II. CFD Simulation of Lift Coefficients for Boomerang Airfoil

Table I provides a representative sample of geometries and launch conditions of boomerangs that are of interest to boomerang enthusiasts that range from novice to world champion. Consider a typical boomerang of 15cm radius, thrown at a translational speed of 20m/s and rotational speed of 10Hz. As illustrated in Fig. 2, for the airfoil segment at the center, the airflow reverses from leading edge to trailing edge when blade crosses 90^0 angle of rotation and switches back to leading edge when the blade crosses 270^0 angle of rotation. Similarly, for the airfoil segment at the tip of the blade, airflow reverses from leading edge to trailing edge when blade crosses ~120^0 angle of rotation and switches back to leading edge when the blade crosses ~240^0 angle of rotation. Furthermore, boomerang wings are typically twisted to have a positive angle-of-attack to generate adequate lift to balance the gravitational force. This results in positive angle-of-attack when the wind hits the leading edge of the boomerang blade; however, as the boomerang blade traverses through the angles where the airflow hits the trailing edge, the angle-of-attack reverses in polarity.

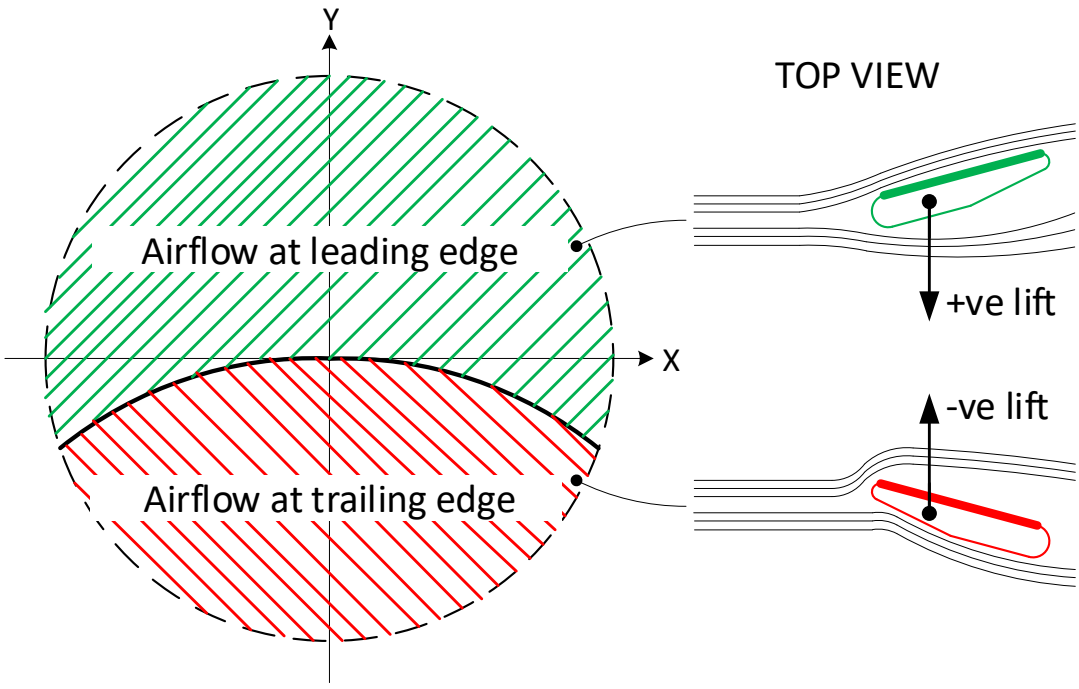

Fig. 2: Illustration of Airflow at Leading Edge Segment vs. Trailing Edge Segment.

Over the last several decades, boomerang designers have experimented with various types of airfoils to maximize the performance of the boomerangs. As illustrated in Fig. 3, these airfoil design modifications fall into two broad categories – undercut and cambered. Undercut design impacts lift and rolling-moment, while cambered design impacts drag. A detailed discussion of this is outside the scope of this work. The reader is referred to [2] for a comprehensive discussion on the impact of undercut and cambered designs on the flight trajectory.

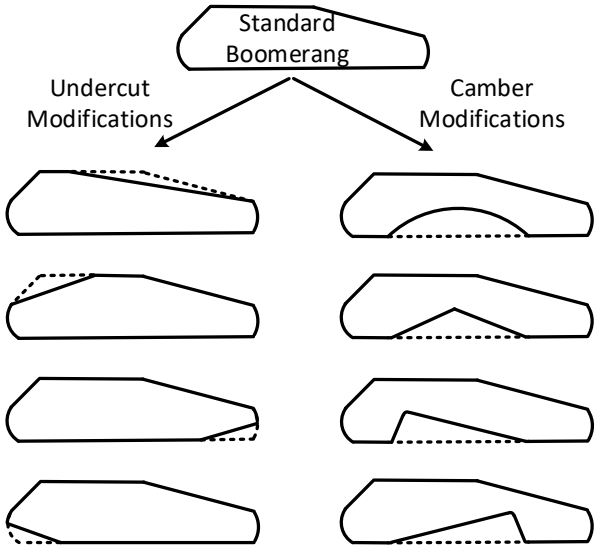

Fig. 3: Examples of Common Boomerang Airfoil Designs.

The lift coefficients for a standard boomerang airfoil design were simulated using XFOIL [10]. XFOIL is a program for the design and analysis of subsonic isolated airfoils. Given the coordinates specifying the shape of a 2D airfoil, Reynolds and Mach numbers, XFOIL can calculate the pressure distribution on the airfoil and hence lift and drag characteristics. Simulations were performed with orientation of the airfoil consistent with the top view illustrated in Fig. 2 for a right-hand throw. The pressure distribution on the leading edge of the airfoil for zero and positive angle-of-attack are shown in Fig. 4 and Fig. 5 respectively. Similarly, the pressure distribution on the trailing edge for the airfoil for zero and negative angle-of-attack are shown in Fig. 6 and Fig. 7 respectively. Airflow to the leading edge with zero and positive angle-of-attack produces positive lift while airflow to the trailing edge with zero and negative angle-of-attack produces negative lift. The reader is advised to pay careful attention to the orientation of the boomerang airfoil in the top view illustrated in Fig. 2 for a right-hand throw for correct interpretation of the direction of lift.

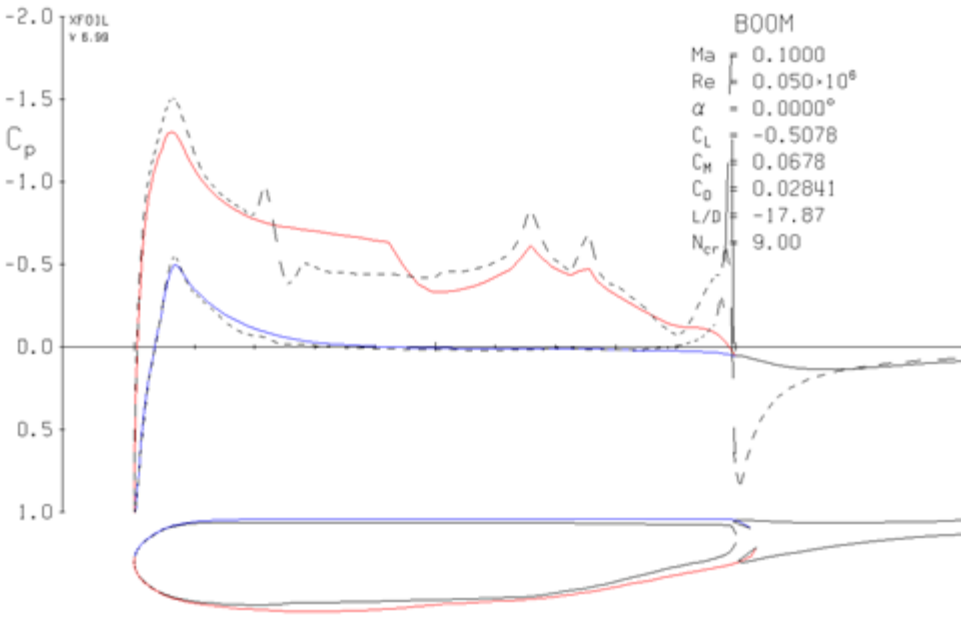

Fig. 4: XFOIL Simulations for the Leading Edge at 0^0 AOA for a Standard Boomerang Airfoil.

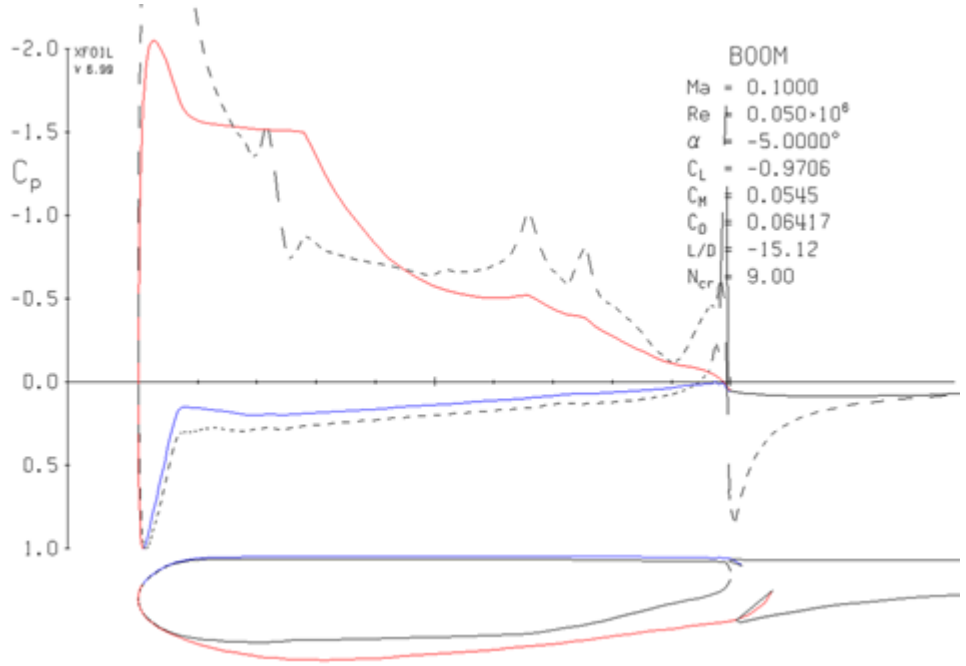

Fig. 5: XFOIL Simulations for the Leading Edge at -5^0 AOA for a Standard Boomerang Airfoil.

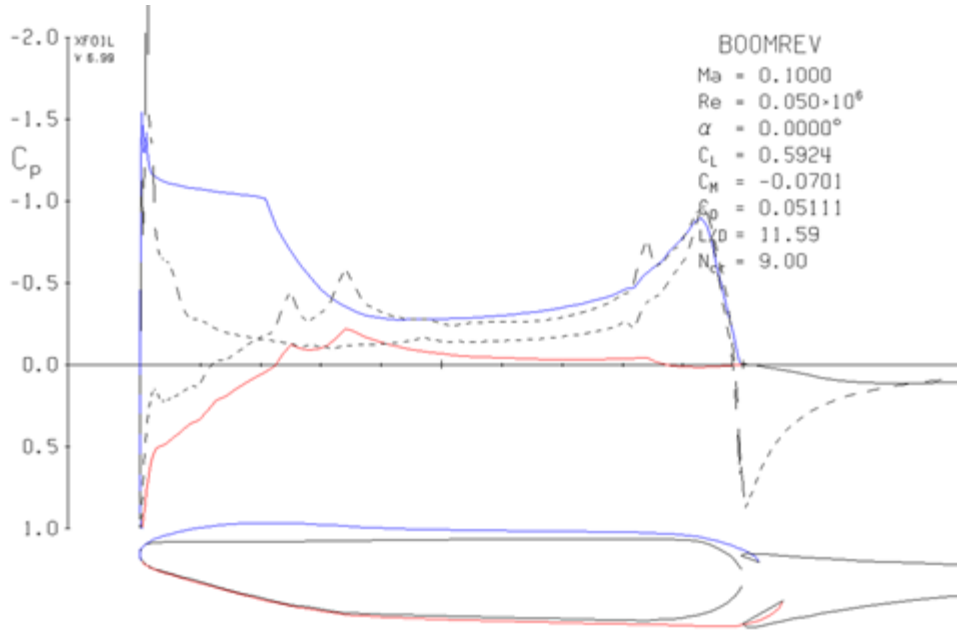

Fig. 6: XFOIL Simulations for the Trailing Edge at 0^0 AOA for Standard Boomerang Airfoil.

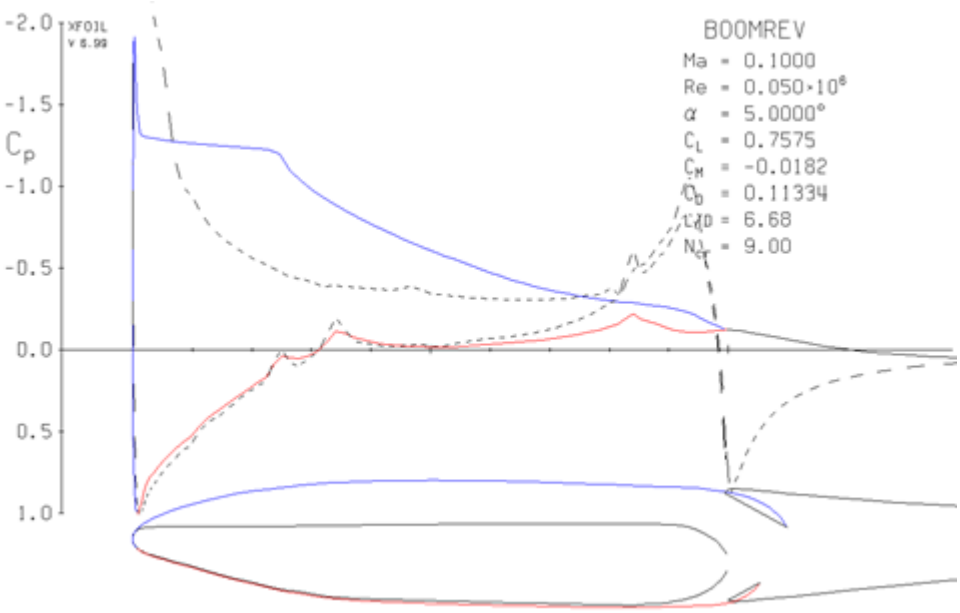

Fig. 7: XFOIL Simulations for the Trailing Edge at $+5^0$ AOA Standard Boomerang Airfoil.

Simulation results of XFOIL for lift coefficients for various positive and negatives angle-of-attack for leading edge and trailing edge are shown in Fig. 8 and Fig. 9. Similarly, simulation results of XFOIL for lift-to-drag coefficients for positive and negatives angle-of-attack for leading edge and trailing edge are shown in Fig. 10 and Fig. 11. The

region of interest in each case is identified for clarity and the direction of lift is to be interpreted to be consistent with the top view illustrated in Fig. 2 for a right-hand throw. It is widely reported in literature that even though XFOIL predicts the trends correctly, it over predicts lift [11]. For example, in [12], it has been reported that XFOIL significantly over predicted lift coefficient for BC2125 (with airfoil similar to standard boomerang airfoil used in this study), at zero angle-of-attack when compared to measurements. It has also been reported that XFOIL underpredicts drag [11]. It is expected similar discrepancies exists in the XFOIL simulation results reported in this work i.e. trends are accurate, but it is desirable to obtain the raw numbers for lift and drag coefficients from experimental data.

Figures 8 and 9 in the next page.

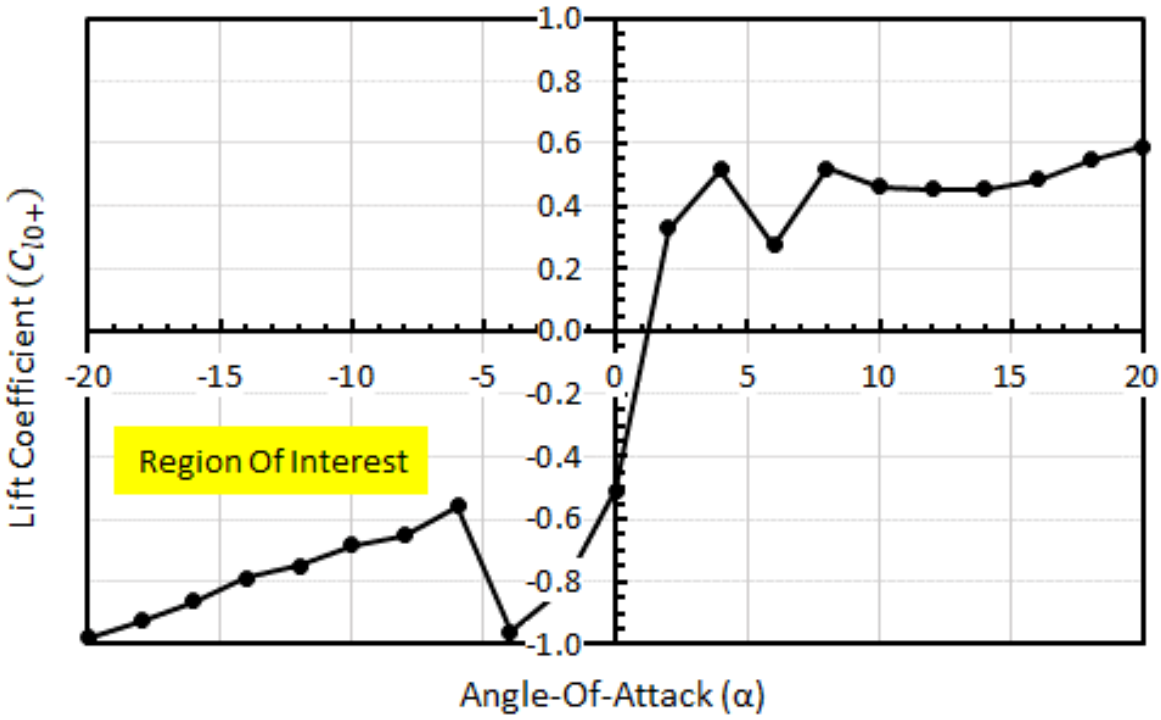

Fig. 8: Lift Coefficients Vs. AOA for the Leading Edge of a Standard Boomerang Airfoil.

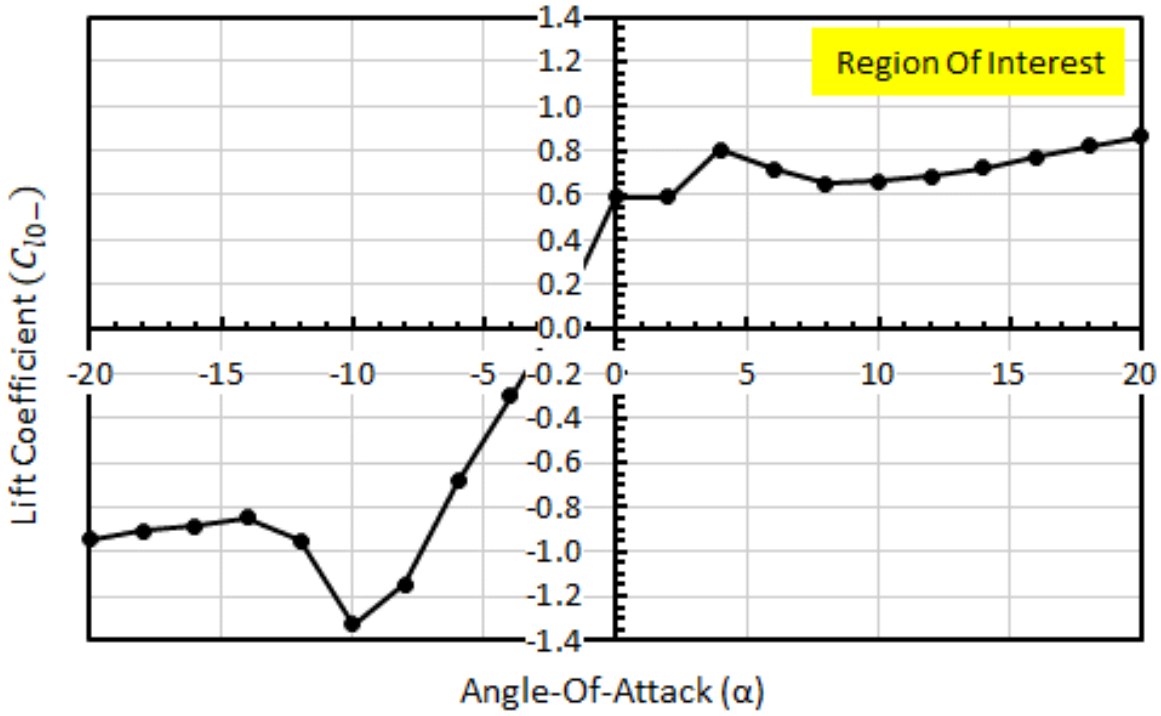

Fig. 9: Lift Coefficients Vs. AOA for the Trailing Edge of a Standard Boomerang Airfoil.

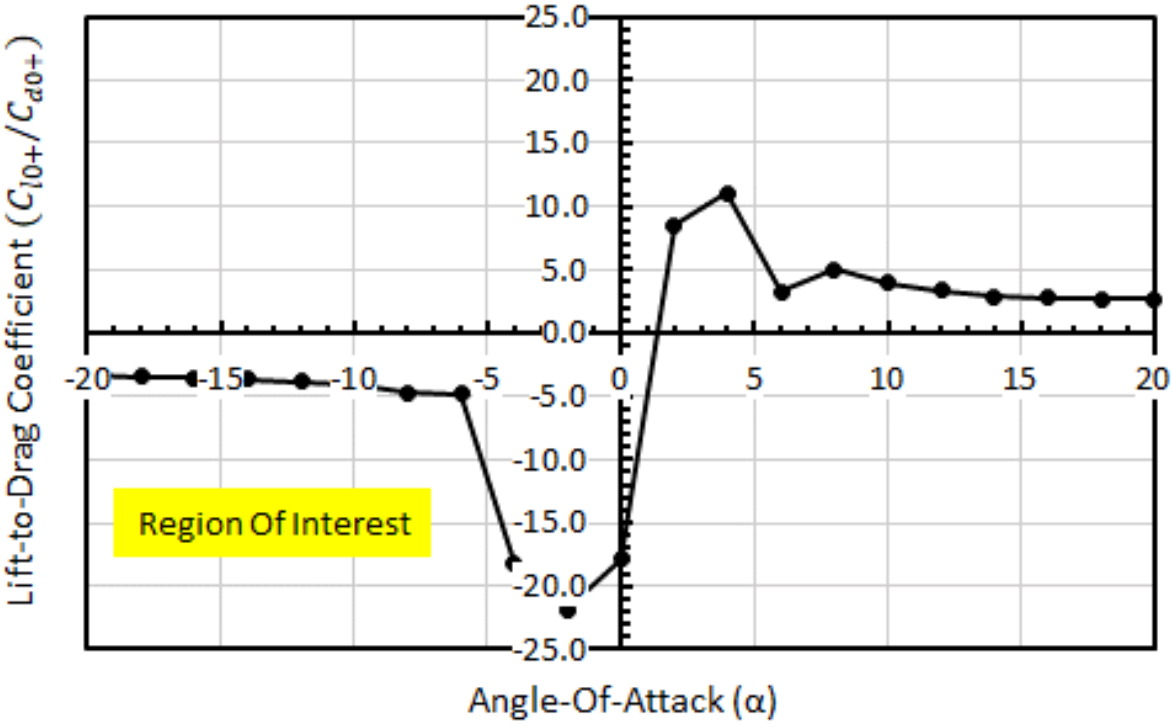

Fig. 10: Lift-to-Drag Coefficient Vs. AOA for the Leading Edge of a Standard Boomerang Airfoil.

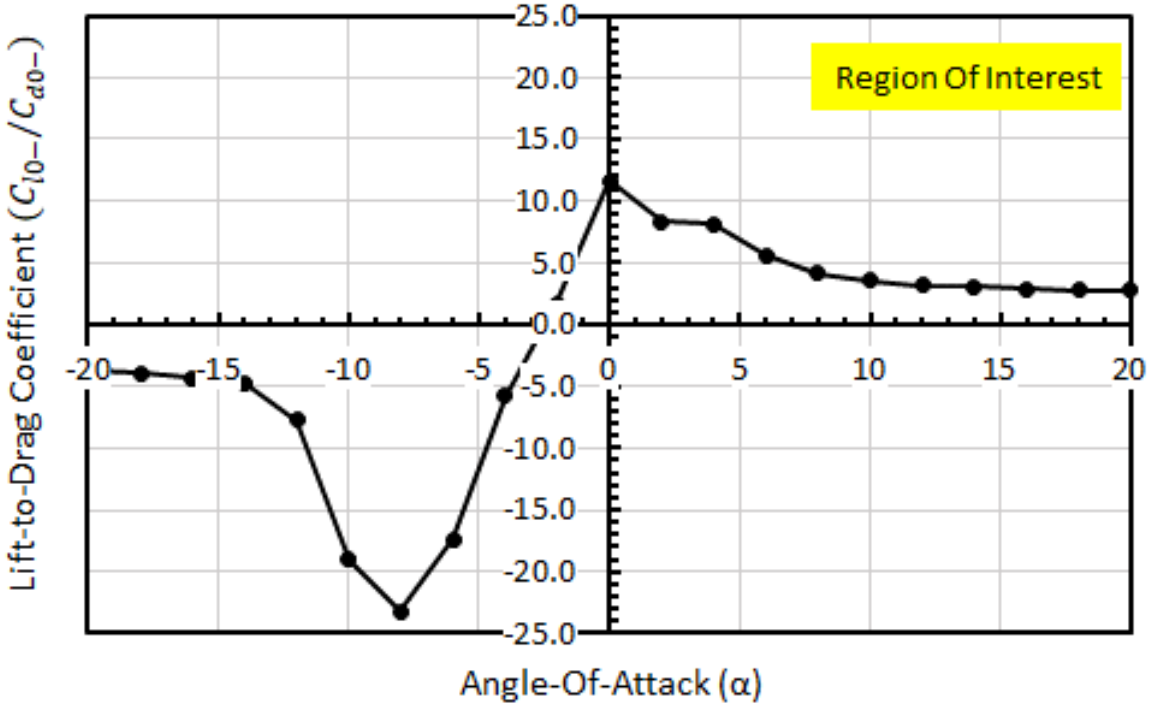

Fig. 11: Lift-to-Drag Coefficient Vs. AOA for the Trailing Edge of a Standard Boomerang Airfoil.

III. Lift and Rolling-Moment for Leading Edge and Trailing Edge

As illustrated in Fig. 12, the translational velocity and the rotation velocity for each blade element can be combined to determine the velocity of the blade element perpendicular (normal) to the wind:

$$V_n(r,\psi) = V\cos(\psi) + r\omega \tag{1}$$

where V is the translational velocity of the boomerang, ω is the angular velocity of the boomerang, ψ is the angle of the blade, r is the segment distance from the center. Using Eq. (1), the region where the blade segments experience airflow from the leading edge vs. trailing edge can be identified. Using the blade-element theory approach outlined in [9], expressions for time-averaged lift and rolling-moment will be developed by integrating the lift generated by each segment of the blade as it traverses 360^0 angle of rotation and over the blade radius. Time-averaged lift for leading edge and trailing edge will be evaluated separately using the appropriate lift coefficient and angle-of-attack. The total time-averaged lift is then determined by combining the lift in both regions. A similar approach is followed to determine the time-averaged rolling-moment.

Based on the initial launch conditions and final return conditions described in Table I, the non-dimensional angular speed at launch is approximately 0.5. As the boomerang progresses in the flight path, the translational speed and rotational speed are both reduced due to drag. Based on observation of the boomerang flight, the translational speed decreases more than the rotational speed (as a percentage). This causes the non-dimensional angular speed to increase but nonetheless it remains close to 1 until the very end of the flight.

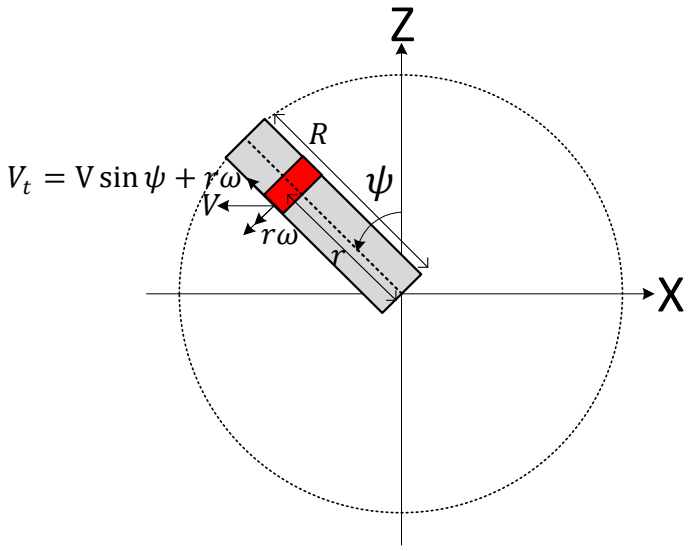

Fig. 12: Vectoral Addition of Translational Velocity and Rotational Velocity of the Blade Segment.

Non-dimensional Lift and Rolling-Moment Coefficient Derivations

Using the blade element theory (BET) approach described in [9], the basic lift for the leading-edge differential segment of the boomerang blade can be expressed as:

$$\begin{aligned} L_0^+(\psi,r) &= \frac{1}{2}\rho V_n^2 C_{l0+} C d\psi dr \\ &= \frac{1}{2}\rho C C_{l0+} [\mathrm{V}\cos\psi + r\omega]^2 d\psi dr \\ &= \frac{1}{2}\rho V^2 C C_{l0+} \left[\cos\psi + \left(\frac{r\chi}{R}\right)\right]^2 d\psi dr \end{aligned} \tag{2}$$

where ρ is the air density, C is the chord length, C_{l0+} is the lift coefficient for leading edge, χ is the non-dimensional rotational speed, R is the radius and ψ is the Euler angle in the n-axis as described in [9]. The time-averaged lift for the leading edge can be determined by integrating the differential lift over the angle of rotation when airflows hits the leading edge and over the length of the blade:

$$\begin{aligned} \overline{L_0^+} &= \int_0^R \left\{ \frac{1}{\pi} \int_0^{\pi - \cos^{-1}\left(\frac{r\chi}{R}\right)} dL_0^+(\psi,r) d\psi \right\} dr \\ &= \frac{1}{2}\rho V^2 C C_{l0+} \int_0^R \left\{ \frac{1}{\pi} \int_0^{\pi - \cos^{-1}\left(\frac{r\chi}{R}\right)} \left[\cos\psi + \left(\frac{r\chi}{R}\right)\right]^2 d\psi \right\} dr \\ &= \frac{1}{2}\rho V^2 C C_{l0+} \int_0^R \left\{ \frac{1}{2} + \left(\frac{r\chi}{R}\right)^2 + \frac{3}{2\pi}\left(\frac{r\chi}{R}\right)\sqrt{1-\left(\frac{r\chi}{R}\right)^2} - \frac{1}{2\pi}\left[1 + 2\left(\frac{r\chi}{R}\right)^2\right]\cos^{-1}\left(\frac{r\chi}{R}\right) \right\} dr \\ &= \frac{1}{2}\rho V^2 R C C_{l0+} \left\{ \frac{1}{2} + \frac{\chi^2}{3} + \frac{1}{2\pi\chi}\left[\sqrt{1-\chi^2} - (1-\chi^2)^{\frac{3}{2}} - \chi\cos^{-1}\chi\right] - \frac{1}{3\pi\chi}\left[\chi^3\cos^{-1}\chi - \frac{1}{3}\left[(2+\chi^2)\sqrt{1-\chi^2} - 2\right]\right] \right\} \end{aligned} \tag{3}$$

Similarly, the time-averaged lift for the trailing edge can be determined by integrating the differential lift over the angle of rotation when airflows hits the trailing edge and over the length of the blade:

$$\begin{aligned} \overline{L_0^-} &= \frac{1}{2}\rho V^2 C C_{l0-} \int_0^R \left\{ \frac{1}{\pi} \int_{\pi - \cos^{-1}\left(\frac{r\chi}{R}\right)}^{\pi} \left[\cos\psi + \left(\frac{r\chi}{R}\right)\right]^2 d\psi \right\} dr \\ &= \frac{1}{2}\rho V^2 C C_{l0-} \int_0^R \left\{ -\frac{3}{2\pi}\left(\frac{r\chi}{R}\right)\sqrt{1-\left(\frac{r\chi}{R}\right)^2} + \frac{1}{2\pi}\left[1 + 2\left(\frac{r\chi}{R}\right)^2\right]\cos^{-1}\left(\frac{r\chi}{R}\right) \right\} dr \\ &= \frac{1}{2}\rho V^2 R C C_{l0-} \left\{ -\frac{1}{2\pi\chi}\left[\sqrt{1-\chi^2} - (1-\chi^2)^{\frac{3}{2}} - \chi\cos^{-1}\chi\right] + \frac{1}{3\pi\chi}\left[\chi^3\cos^{-1}\chi - \frac{1}{3}\left[(2+\chi^2)\sqrt{1-\chi^2} - 2\right]\right] \right\} \end{aligned} \tag{4}$$

The total time-averaged lift can be obtained by adding the time-averaged lift over the leading edge and trailing edge:

$$\begin{aligned}\overline{L_0} &= \overline{L_0^+} + \overline{L_0^-} \\ &= \frac{1}{2}\rho V^2 R C C_{l0+}\left\{\left[\frac{1}{2}+\frac{\square^2}{3}\right]\right. \\ &\qquad + \left(1-\frac{C_{l0-}}{C_{l0+}}\right)\left[\frac{1}{2\pi\chi}\left[\sqrt{1-\chi^2}-(1-\chi^2)^{\frac{3}{2}}-\chi\cos^{-1}\chi\right]\right. \\ &\qquad \left.\left.-\frac{1}{3\pi\chi}\left[\chi^3\cos^{-1}\chi-\frac{1}{3}\left[(2+\chi^2)\sqrt{1-\chi^2}-2\right]\right]\right]\right\}\end{aligned} \tag{5}$$

Using eq. (5), the non-dimensional basic lift coefficient can be expressed as:

$$\overline{C_{L0}} = \left[\frac{1}{2}+\frac{\chi^2}{3}\right] + \left(1-\frac{C_{l0-}}{C_{l0+}}\right)\left[\frac{1}{2\pi\chi}\left[\sqrt{1-\chi^2}-(1-\chi^2)^{\frac{3}{2}}-\chi\cos^{-1}\chi\right]-\frac{1}{3\pi\chi}\left[\chi^3\cos^{-1}\chi-\frac{1}{3}\left[(2+\chi^2)\sqrt{1-\chi^2}-2\right]\right]\right] \tag{6}$$

Using a similar approach, coefficients for non-dimensional angle-of-attack lift ($\overline{\boldsymbol{C_{L\alpha}}}$), non-dimensional basic rolling-moment ($\overline{\boldsymbol{C_{MX0}}}$) and non-dimensional angle-of-attack rolling-moment ($\overline{\boldsymbol{C_{MX\alpha}}}$) can be expressed as:

$$\overline{C_{L\alpha}} = \frac{\chi}{2}+\frac{1}{2\pi}\left(1+\frac{C_{l\alpha-}}{C_{l\alpha+}}\right)\left[\frac{3}{2}\sqrt{1-\chi^2}+\frac{\sin^{-1}\chi}{2\chi}-\chi\cos^{-1}\chi\right] \tag{7}$$

$$\begin{aligned}\overline{C_{MX0}} = \frac{\chi}{3}+\frac{1}{3}\left(1-\frac{C_{l0-}}{C_{l0+}}\right)&\left[\frac{1}{15\pi\chi^2}\left[2+(3\chi^4-\chi^2-2)\sqrt{1-\chi^2}\right]+\frac{2}{3\pi\chi^2}\left[1-(1-\chi^2)^{3/2}\right]\right. \\ &\left.-\frac{1}{\pi}\left[\chi\cos^{-1}\chi-\frac{1}{3\chi^2}\left[(2+\chi^2)\sqrt{1-\chi^2}-2\right]\right]\right]\end{aligned} \tag{8}$$

$$\overline{C_{MX\alpha}} = \frac{1}{4}+\left(1+\frac{C_{l\alpha-}}{C_{l\alpha+}}\right)\left[\frac{1}{16\pi\chi}\left[(2\chi^2-1)\sqrt{1-\chi^2}+\frac{\sin^{-1}\chi}{\chi}\right]-\frac{1}{8\pi\chi}\left[\frac{\sin^{-1}\chi}{\chi}+2\chi\cos^{-1}\chi-\sqrt{1-\chi^2}\right]\right] \tag{9}$$

Equations in [9] for time-averaged basic lift, angle-of-attack lift, basic rolling-moment and angle-of-attack rolling-moment, can be readily obtained from Eqns. 6-9 by setting $C_{l0+} = C_{l0-}$ and $C_{l\alpha+} = C_{l\alpha-}$. Although Eqns. 6-9 were derived assuming $\chi < 1$ the results can be readily applied for $\chi > 1$ by taking the real part of the expressions on the right-hand side.

The non-dimensional basic lift coefficient ($\overline{C_{L0}}$), non-dimensional angle-of-attack lift coefficient ($\overline{C_{L\alpha}}$), non-dimensional basic rolling-moment coefficient ($\overline{C_{MX0}}$) and non-dimensional angle-of-attack rolling-moment coefficient ($\overline{C_{MX\alpha}}$) were plotted as a function of non-dimensional angular speed (χ) in Figs. 13-16. Plots for $C_{l0-}/C_{l0+} = +1$ correspond to the expressions derived in [9] without considering the reversal of airflow and reversal of angle-of-attack. Based on the XFOIL simulation results in section II, $C_{l0-}/C_{l0+} \sim -1$ for the standard boomerang airfoil. Plots for

$C_{l0-}/C_{l0+} = -1$ corresponds to Eqns. 6-9 which consider the reversal of airflow and reversal of angle-of-attack. Comparison of results for $C_{l0-}/C_{l0+} = +1$ with results for $C_{l0-}/C_{l0+} = -1$ highlights the expected impact of considering the reversal of airflow and reversal of angle-of-attack on the lift, pitching-moments and rolling-moment that impact the aerodynamics of boomerangs. Percentage error in the estimation of $\overline{C_{L0}}$, $\overline{C_{L\alpha}}$, $\overline{C_{MX0}}$, $\overline{C_{MX\alpha}}$, $\overline{C_{MY0}}$, $\overline{C_{MY\alpha}}$ with and without considering the reversal of airflow and reversal of angle-of-attack are plotted in Fig. 17. These results can be summarized as follows: average of ~50% error at non-dimensional angular speed of 0.5 that decreases to an average of ~30% at non-dimensional angular speed of 1.0 and rapidly approaches 0% for non-dimensional angular speeds of 2.0 and higher.

Figures 13 and 14 in the next page.

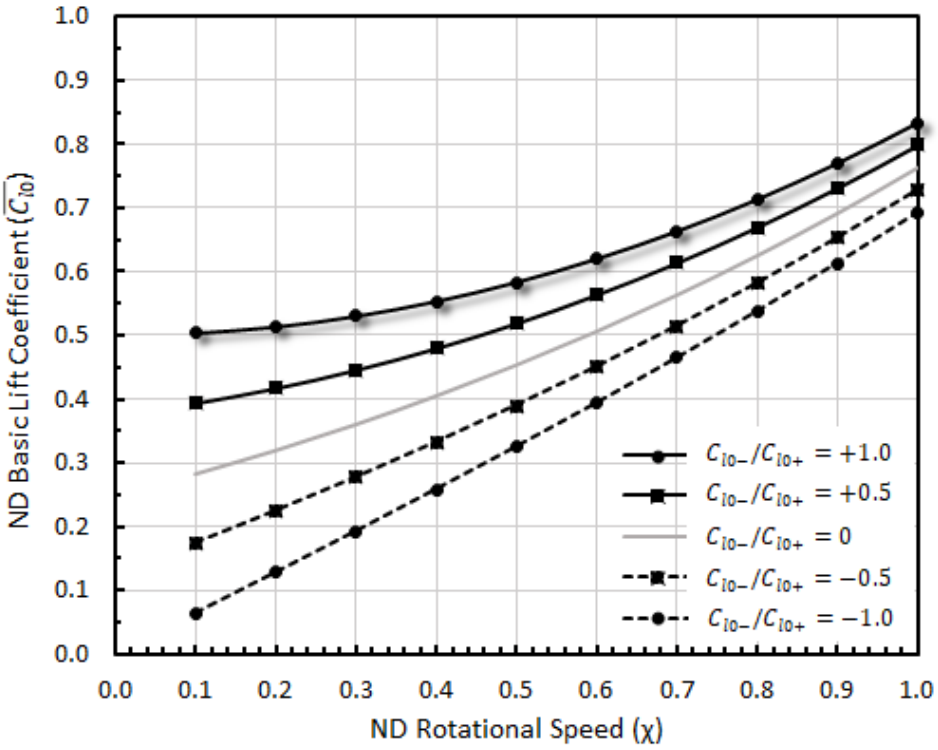

Fig. 13: Non-Dimensional Basic Lift Coefficient ($\overline{C_{L0}}$) vs. Non-Dimensional Angular Speed (χ).

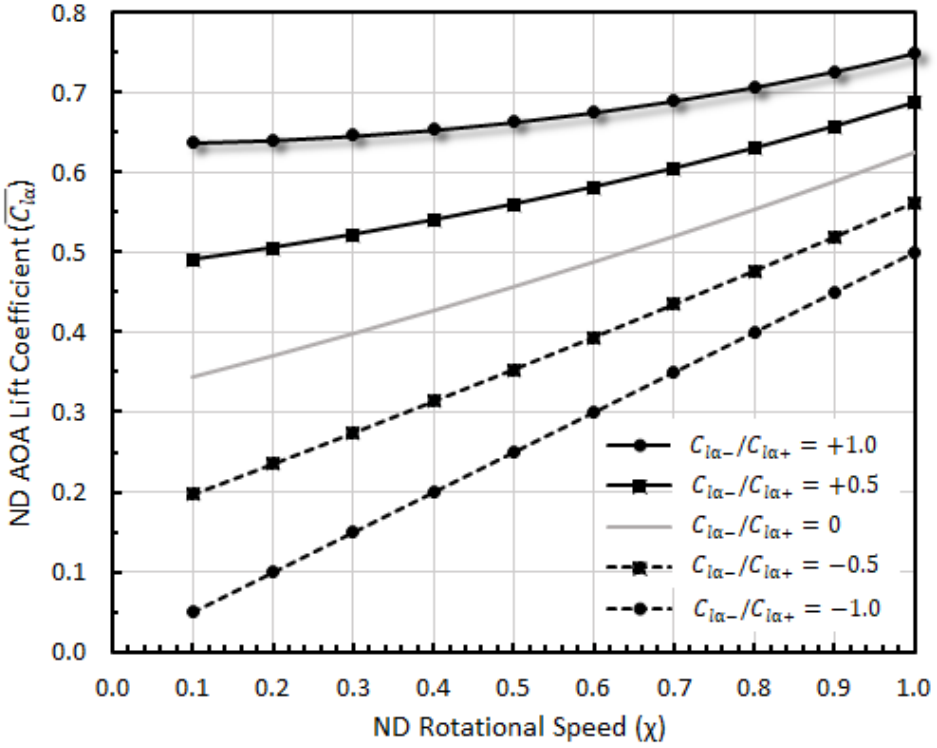

Fig. 14: Non-Dimensional AOA Lift Coefficient ($\overline{C_{L\alpha}}$) vs. Non-Dimensional Angular Speed (χ).

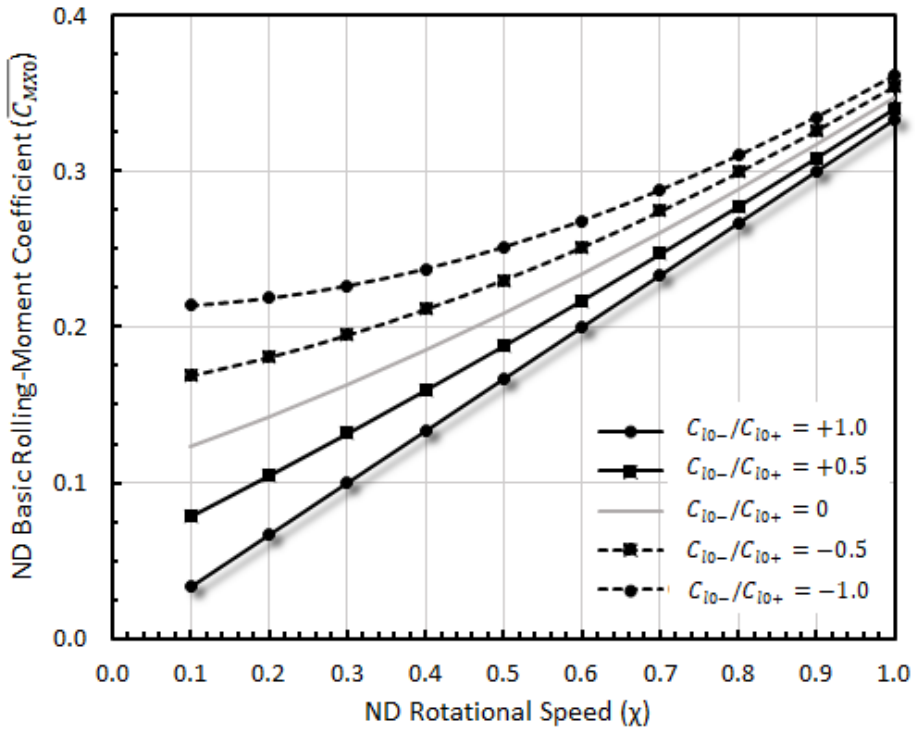

Fig. 15: Non-Dimensional Basic Rolling-Moment Coefficient ($\overline{C_{MX0}}$) vs. Non-Dimensional Angular Speed (χ).

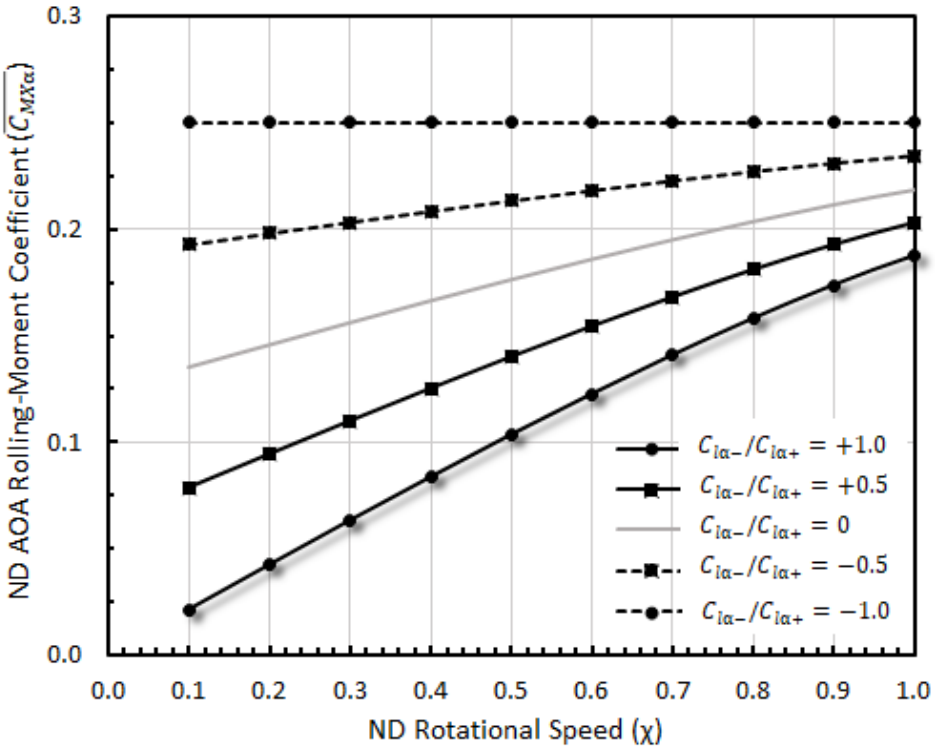

Fig. 16: Non-Dimensional AOA Rolling-Moment Coefficient ($\overline{C_{MX\alpha}}$) vs. Non-Dimensional Angular Speed (χ).

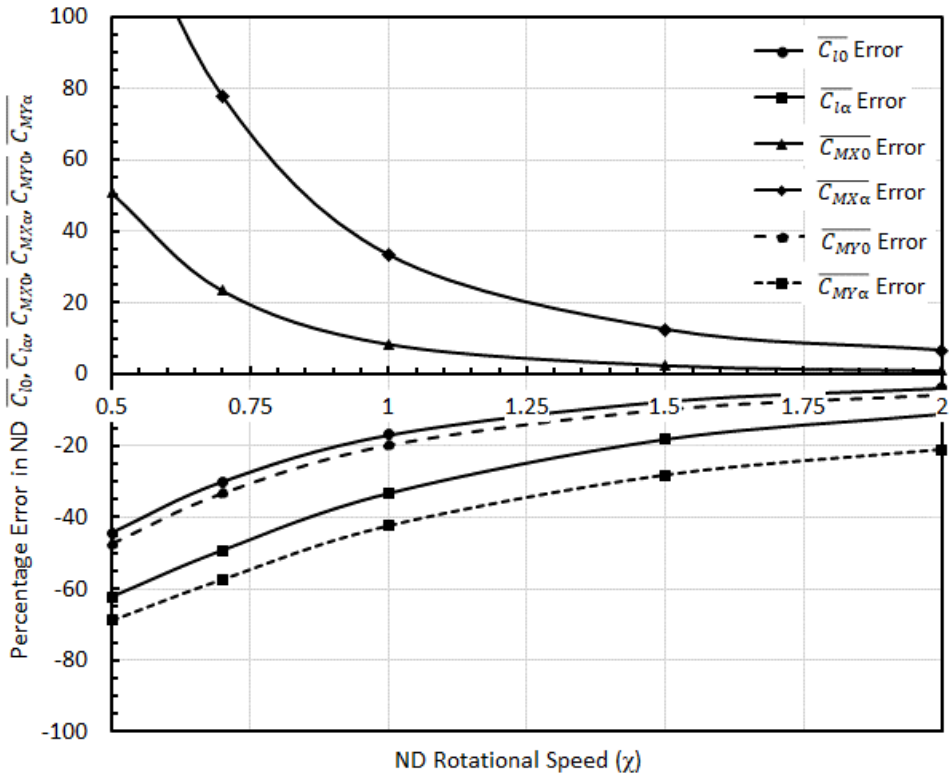

Fig. 17: Percentage Error In Prediction Of $\overline{C_{L0}}$, $\overline{C_{L\alpha}}$, $\overline{C_{MX0}}$, $\overline{C_{MX\alpha}}$, $\overline{C_{MY0}}$, $\overline{C_{MY\alpha}}$ vs. Non-Dimensional Angular Speed (χ).

Discussion of pitching-moment in the next page.

Pitching-Moment Derivation

As illustrated in Fig. 18, lift in airfoils is generated at an offset from the axis of symmetry of the blade. Furthermore, when the airflow reverses from leading edge to trailing edge the lift switches from leading edge to the trailing edge across the axis of symmetry. Using Fig. 18, it is possible to readily conclude that the time-averaged pitching-moment is not zero. Interestingly, even if reversal of airflow from leading edge to trailing edge is ignored, it is to be noted that pitching-moment is not zero. This is contrary to the conclusion reported in [9]. The pitching-moment derivation that follows confirms the conclusions of the visualization in Fig. 18.

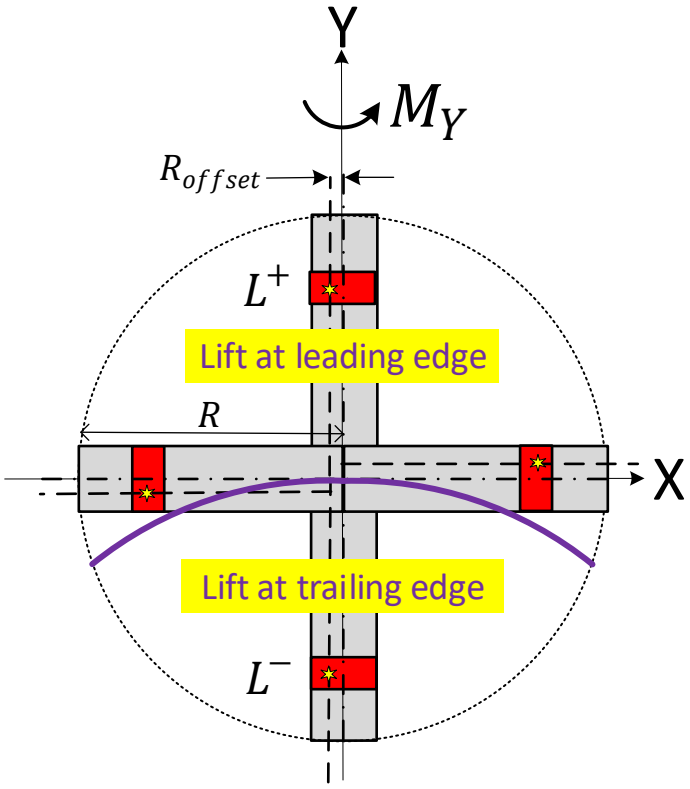

Fig. 18: Illustration of Pitching-Moment.

The basic pitching-moment for the leading-edge differential segment of the boomerang blade can be expressed as:

$$M_{Y0}^{+}(\psi, r) = \frac{1}{2}\rho V_n^2 C_{l0+} C . R_{offset} . \cos\psi \, d\psi dr$$

$$= \frac{1}{2}\rho V^2 C C_{l0+} R_{offset} \left[\cos\psi + \left(\frac{r\chi}{R}\right)\right]^2 \cos\psi \, d\psi dr \quad (10)$$

The time-averaged pitching-moment for the leading edge can be determined by integrating the Eq. 10 over the angle of rotation when airflows hits the leading edge and over the length of the blade:

$$\overline{M_{Y0}^{+}} = \frac{1}{2}\rho V^2 C C_{l0+} R_{offset} \int_0^R \left\{ \frac{1}{\pi} \int_0^{\pi - \cos^{-1}\left(\frac{r\chi}{R}\right)} \left[\cos\psi + \left(\frac{r\chi}{R}\right)\right]^2 \cos\psi \, d\psi \right\} dr$$

$$= \frac{1}{2}\rho V^2 C C_{l0+} R_{offset} \int_0^R \frac{1}{3\pi} \left\{ 3\pi \left(\frac{r\chi}{R}\right) + \left[2 + \left(\frac{r\chi}{R}\right)^2\right] \sqrt{1 - \left(\frac{r\chi}{R}\right)^2} - 3\left(\frac{r\chi}{R}\right) \cos^{-1}\left(\frac{r\chi}{R}\right) \right\} dr$$

$$= \frac{1}{2}\rho V^2 R C C_{l0+} R_{offset} \left\{ \frac{\chi}{2} + \frac{1}{3\pi}\left[\sqrt{1-\chi^2} + \frac{\sin^{-1}\chi}{\chi}\right] + \frac{1}{24\pi}\left[(2\chi^2 - 1)\sqrt{1-\chi^2} + \frac{\sin^{-1}\chi}{\chi}\right] \right.$$

$$\left. - \frac{1}{4\pi}\left[\frac{\sin^{-1}\chi}{\chi} + 2\chi\cos^{-1}\chi - \sqrt{1-\chi^2}\right] \right\} \tag{11}$$

Similarly, the time-averaged pitching-moment for the trailing edge can be written as:

$$\overline{M_{Y0}^{-}} = \frac{1}{2}\rho V^2 C C_{l0-} \left(-R_{offset}\right) \int_0^R \left\{ \frac{1}{\pi} \int_{\pi - \cos^{-1}\left(\frac{r\chi}{R}\right)}^{\pi} \left[\cos\psi + \left(\frac{r\chi}{R}\right)\right]^2 \cos\psi \, d\psi \right\} dr$$

$$= -\frac{1}{2}\rho V^2 C C_{l0-} R_{offset} \int_0^R \frac{1}{3\pi} \left\{ \left[2 + \left(\frac{r\chi}{R}\right)^2\right] \sqrt{1 - \left(\frac{r\chi}{R}\right)^2} - 3\left(\frac{r\chi}{R}\right) \cos^{-1}\left(\frac{r\chi}{R}\right) \right\} dr$$

$$= -\frac{1}{2}\rho V^2 R C C_{l0-} R_{offset} \left\{ -\frac{1}{3\pi}\left[\sqrt{1-\chi^2} + \frac{\sin^{-1}\chi}{\chi}\right] - \frac{1}{24\pi}\left[(2\chi^2 - 1)\sqrt{1-\chi^2} + \frac{\sin^{-1}\chi}{\chi}\right] \right.$$

$$\left. + \frac{1}{4\pi}\left[\frac{\sin^{-1}\chi}{\chi} + 2\chi\cos^{-1}\chi - \sqrt{1-\chi^2}\right] \right\} \tag{12}$$

Combining Eqns. 11 and 12, the non-dimensional pitching-moment coefficient can be expressed as:

$$\overline{C_{MY0}} = \frac{\chi}{2} + \left(1 + \frac{C_{l0-}}{C_{l0+}}\right)\left[\frac{1}{3\pi}\left[\sqrt{1-\chi^2} + \frac{\sin^{-1}\chi}{\chi}\right] + \frac{1}{24\pi}\left[(2\chi^2 - 1)\sqrt{1-\chi^2} + \frac{\sin^{-1}\chi}{\chi}\right] \right.$$

$$\left. - \frac{1}{4\pi}\left[\frac{\sin^{-1}\chi}{\chi} + 2\chi\cos^{-1}\chi - \sqrt{1-\chi^2}\right]\right] \tag{13}$$

Similarly, the non-dimensional angle-of-attack pitching-moment coefficient can be expressed as:

$$\overline{C_{MY\alpha}} = \frac{1}{2} + \left(1 - \frac{C_{l\alpha-}}{C_{l\alpha+}}\right)\left[\frac{1}{6\pi\chi}\left[1 - (1-\chi^2)^{\frac{3}{2}}\right] - \frac{1}{2\pi\chi}\left[1 + \chi\cos^{-1}\chi - \sqrt{1-\chi^2}\right]\right] \tag{14}$$

The non-dimensional basic pitching-moment coefficient ($\overline{C_{MY0}}$) and non-dimensional angle-of-attack pitching-moment coefficient ($\overline{C_{MY\alpha}}$) were plotted as a function of non-dimensional angular speed (χ) in Figs. 19 and 20. These results validate the earlier conclusions that the time-averaged pitching-moment is not zero. Furthermore, the time-averaged pitching-moment remains non-zero even if reversal of airflow from leading edge to trailing edge is neglected ($C_{l0-}/C_{l0+} = +1$).

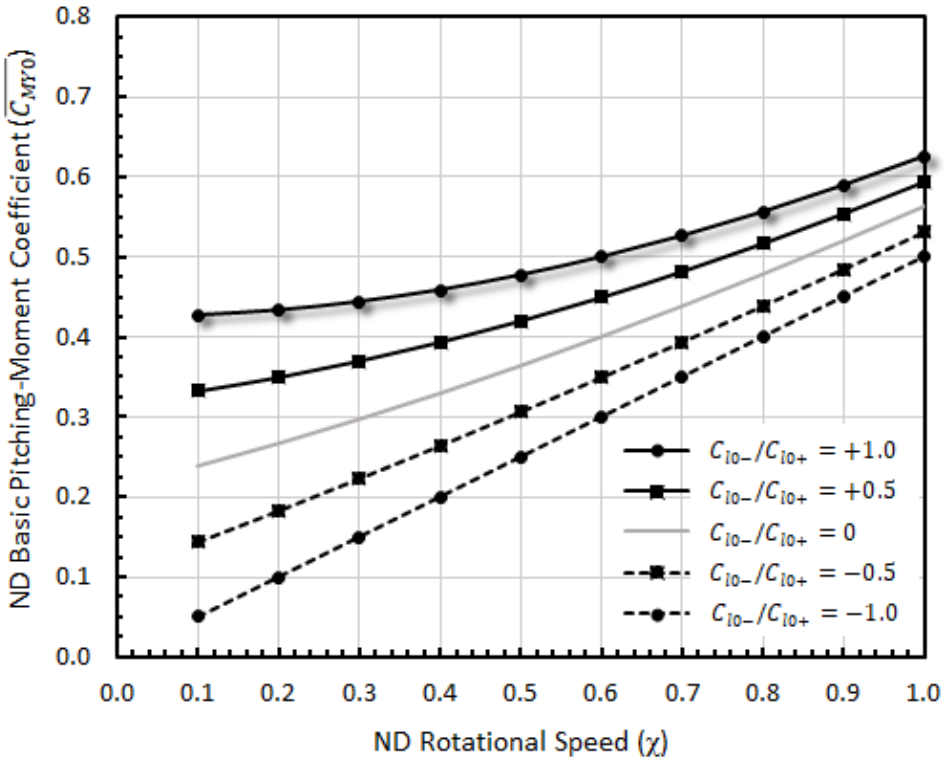

Fig. 19: Non-Dimensional Basic Pitching-Moment Coefficient ($\overline{C_{MY0}}$) vs. Non-Dimensional Angular Speed (χ).

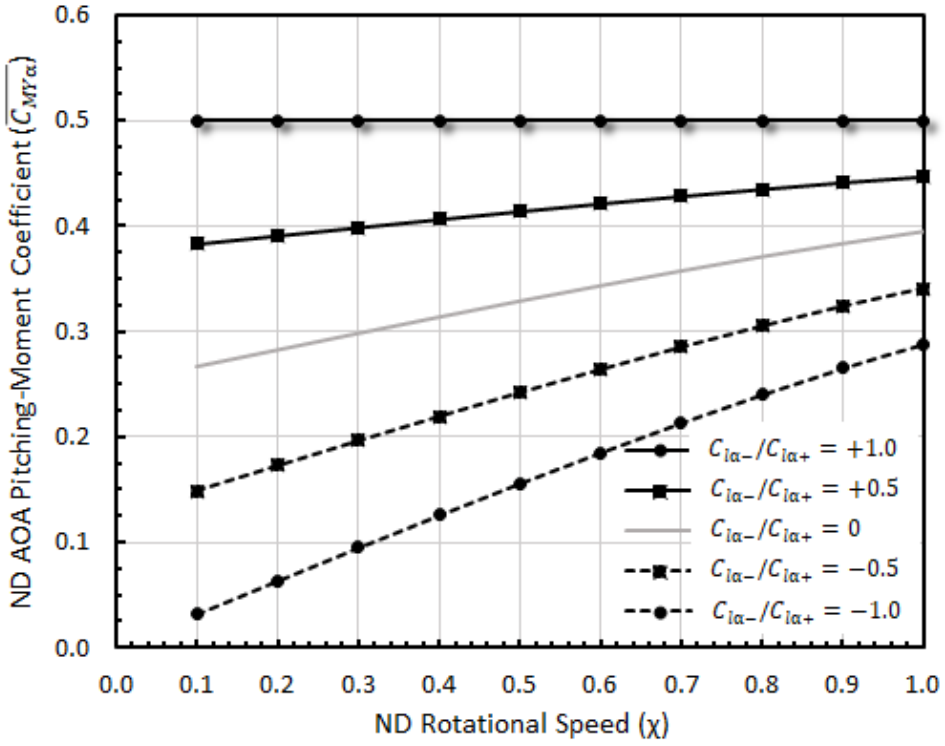

Fig. 20: Non-Dimensional AOA Pitching-Moment Coefficient ($\overline{C_{M\alpha}}$) vs. Non-Dimensional Angular Speed (χ).

Simplified Expressions for Lift, Rolling-Moment and Pitching-Moment

The complexity of Eqns. 6-9 and 13-14, obfuscates the weak non-linear dependence of non-dimensional aerodynamic coefficients ($\overline{C_{L0}}$, $\overline{C_{L\alpha}}$, $\overline{C_{MX0}}$, $\overline{C_{MX\alpha}}$, $\overline{C_{MY0}}$, $\overline{C_{MY\alpha}}$) on non-dimensional angular speed (χ). The weak non-linear dependence is evident in Figs 13-16, 19 and 20. Eqns. 6-9 and 13-14 can be simplified using Taylor series expansion. The coefficient of the second-order term were modified to account for truncation of the higher-order terms while providing a good fit for the useful range of $0.5 < \chi < 2$:

$$\overline{C_{L0}} \approx \left[\frac{1}{2}+\frac{\chi^2}{3}\right]-\left(1-\frac{C_{l0-}}{C_{l0+}}\right)\left[\frac{1}{4}-\frac{\chi}{\pi}+\frac{\chi^2}{7}\right] \tag{15}$$

$$\overline{C_{L\alpha}} = \frac{\chi}{2}+\left(1+\frac{C_{l\alpha-}}{C_{l\alpha+}}\right)\left[\frac{1}{\pi}-\frac{\chi}{4}+\frac{\chi^2}{5\pi}\right] \tag{16}$$

$$\overline{C_{MX0}} = \frac{\chi}{3}+\frac{1}{3}\left(1-\frac{C_{l0-}}{C_{l0+}}\right)\left[\frac{1}{\pi}-\frac{\chi}{2}+\left(\frac{3}{4\pi}\right)\chi^2\right] \tag{17}$$

$$\overline{C_{MX\alpha}} = \frac{1}{4}-\left(1+\frac{C_{l\alpha-}}{C_{l\alpha+}}\right)\left[\frac{1}{8}-\frac{\chi}{3\pi}+\frac{\chi^3}{30\pi}\right] \tag{18}$$

$$\overline{C_{MY0}} = \frac{\chi}{2}+\left(1+\frac{C_{l0-}}{C_{l0+}}\right)\left[\frac{2}{3\pi}-\frac{\chi}{4}+\frac{\chi^2}{3\pi}\right] \tag{19}$$

$$\overline{C_{MY\alpha}} = \frac{1}{2}-\left(1-\frac{C_{l\alpha-}}{C_{l\alpha+}}\right)\left[\frac{1}{4}-\frac{\chi}{2\pi}+\frac{\chi^3}{24\pi}\right] \tag{20}$$

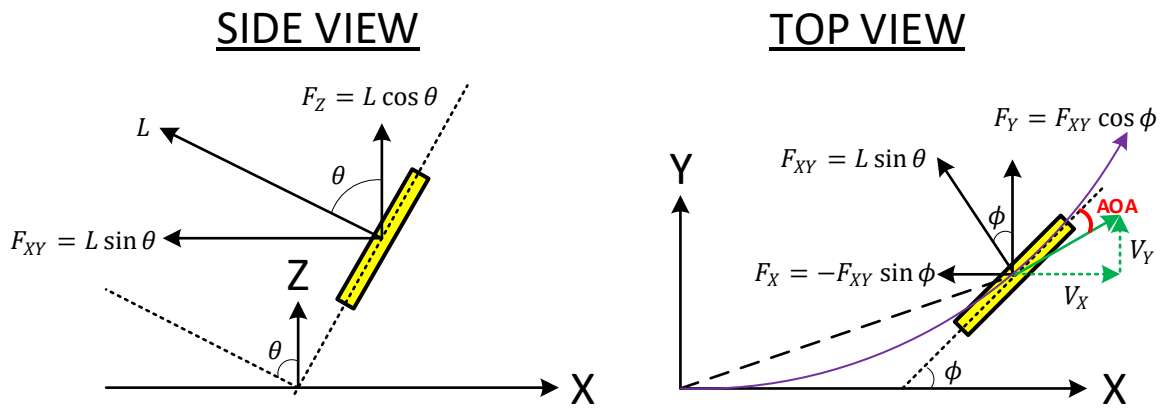

Fig. 21: Illustration of Forces Acting on the Boomerang in (a) Side View and (b) Top View.

IV.Boomerang Flight Trajectory

As illustrated in Fig. 21(a), for a level flight path, the vertical component of the lift generated by the translational and rotational velocities is balanced by the gravitational force on the boomerang.

$$F_Z = L\cos\theta = mg \tag{21}$$

As illustrated in Fig. 21(b), the horizontal component of the lift results in acceleration of the boomerang in the 2D X-Y plane governed by the equations:

$$F_{XY} = L\sin\theta = mg\tan\theta \tag{22}$$

$$\dot{V}_X = \frac{F_X}{m} = -\frac{F_{XY}\sin\phi}{m} = -g\tan\theta\sin\phi \tag{23}$$

$$\dot{V}_Y = \frac{F_Y}{m} = \frac{F_{XY}\cos\phi}{m} = g\tan\theta\cos\phi \tag{24}$$

Euler's equations for angular motion without restriction of $I_X = I_Y$ can be derived following the approach described in [13]. These are a general form of Eq. (9) in [9]. These equations can be summarized as:

$$I_X\ddot{\theta} - I_Y\dot{\phi}^2\sin\theta\cos\theta + I_Z\dot{\phi}\sin\theta\left(\dot{\phi}\cos\theta + \dot{\psi}\right) = M_X \tag{25}$$

$$I_X\dot{\theta}\dot{\phi}\cos\theta + I_Y\left(\ddot{\phi}\sin\theta + \dot{\theta}\dot{\phi}\cos\theta\right) - I_Z\,\dot{\theta}\left(\dot{\phi}\cos\theta + \dot{\psi}\right) = M_Y \tag{26}$$

$$-I_X\dot{\theta}\dot{\phi}\sin\theta + I_Y\dot{\theta}\dot{\phi}\sin\theta + I_Z\left(-\dot{\theta}\dot{\phi}\sin\theta + \ddot{\phi}\cos\theta + \ddot{\psi}\right) = M_Z \tag{27}$$

Eqns. 23 and 24 for translational motion can be combined with Eqns. 25-27 for angular motion to simulate the 2D flight trajectory of the boomerang. Simulation results for nutation angle with and without pitching-moment (Eq. 13) are shown in Fig. 22. Lift is assumed to be offset at one-fourth the chord length. As expected, including pitch-moment results in nutation (layover) of the boomerang. The boomerang nutates ~20^0 from an initial launch angle of 75^0 to return angle of 55^0. A standard boomerang described in Table I was used in the simulation. However, in practice such a boomerang is observed to nutate ~60^0. Other sources of pitching-moment some of which are described in [9], contribute to the additional nutation observed in practice. The authors are currently investigating these sources that contribute to additional nutation and expect to report the findings in a subsequent publication. These additional sources of nutation are emulated by doubling M_Y to illustrate the impact. As expected, the nutation increases getting closer the observations in the field.

As shown in Fig. 23, the flight trajectory of the boomerang is circular when pitching-moment is set to zero. However, when pitching-moment is included using Eq. 13, the boomerang follows an elliptical (or "tear" drop) flight trajectory. Also, the elliptical path is shifted towards the direction of the initial throw. Throw reaches 2m farther in

the positive X-direction but 2m shorter in the negative X-direction. Furthermore, if the additional sources of nutation are emulated by doubling M_Y, the flight trajectory becomes more elliptical closely resembling the flight trajectory in the field.

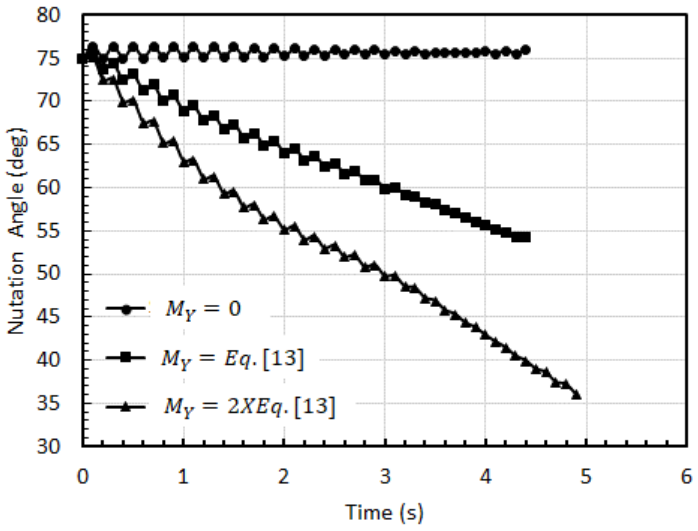

Fig. 22: Nutation Angle vs. Time with and without Pitching-Moment Included.

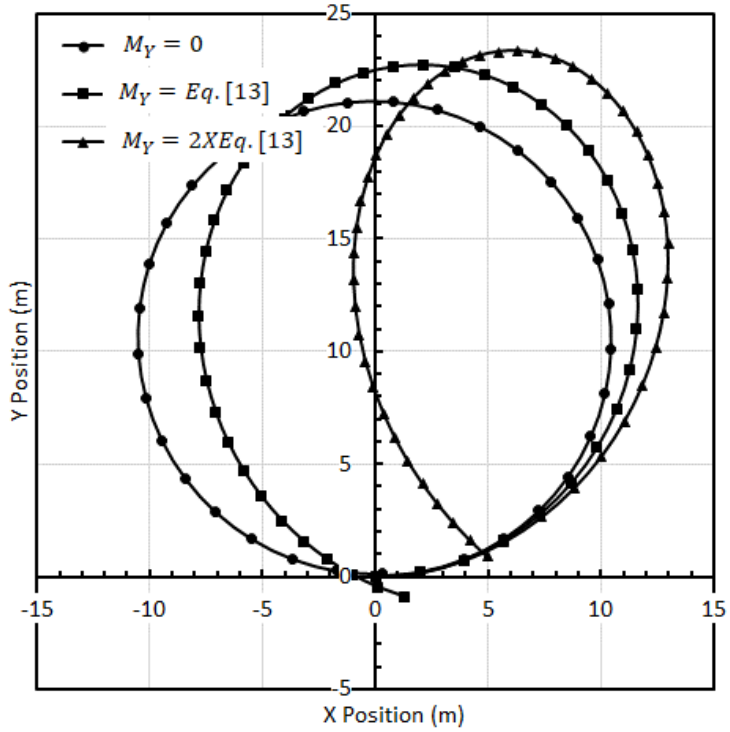

Fig. 23: Flight Trajectory with and without Pitching-Moment Included.

Fig. 24 shows the impact of including the reversal of airflow on the boomerang flight trajectory. Including the reversal of airflow ($C_{l0-}/C_{l0+} = 0, -1$) reduces the rolling-moment. Reduction in the rolling-moment results in the boomerang maintaining a larger radius of curvature causing the boomerang to return to the thrower in a less elliptical and more circular flight path. The precise reduction of rolling-moment depends on the lift coefficients of leading edge vs. trailing edge used in equations for rolling-moment described in the section III. In practice, the thrower compensates for the difference by adjusting the speed of translational speed, rotational speed and launch angle to return the boomerang to the thrower.

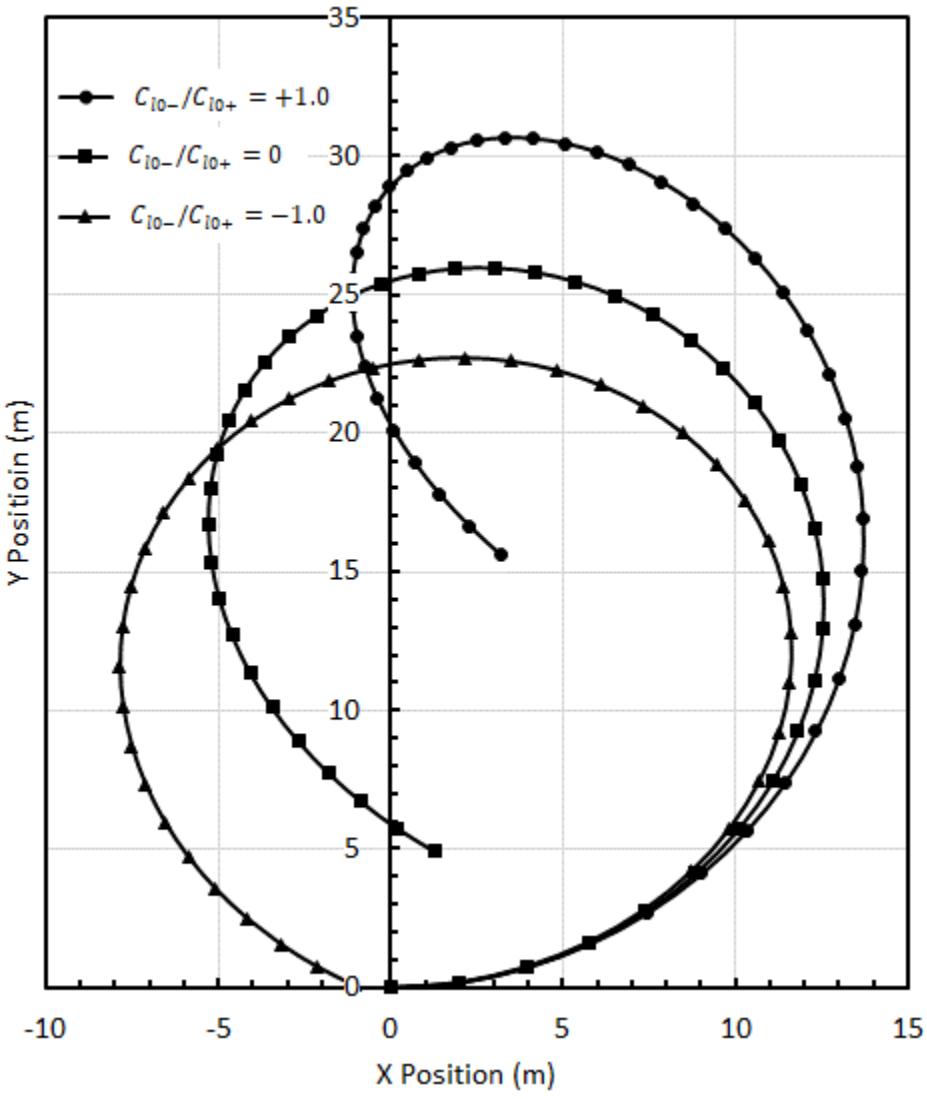

Fig. 24: Flight Trajectory with and without Including Reversal of Airflow from Leading Edge to Trailing Edge.

V. Conclusion

Blades of a boomerang experience reversal of airflow and reversal of angle-of-attack as they traverse the 360-rotation angle. The blade-element-theory approach developed in prior work was used to derive expressions for lift and rolling-moment including the impact of reversal of airflow and reversal of angle-of-attack. Our study shows that the time-averaged lift and rolling-moment are reduced due to reversal of polarity of lift when the air flows over the trailing edge. The impact of reduction in rolling-moment on the flight trajectory of the boomerang was studied and shown to reduce the curvature of the flight path. In addition, an expression for the pitching-moment was derived considering the asymmetric position of lift with respect to axis of symmetry of the blade of a boomerang *and* switches polarity across the axis of symmetry when the airflow switches from leading edge to trailing edge. Contrary to the conclusions in earlier work, our analysis shows that pitching-moment is not zero. Including the pitching-moment leads to nutation (layover) during the boomerang flight of the boomerang. In addition, it leads to an elliptical ("tear drop") flight trajectory. Both these features are consistent with the observation of the flight of a boomerang. Further study is required to explain the larger nutation observed in practice during the flight of a boomerang. Finally, it is noted that the theory developed here is applicable to lightweight fast-moving drones that are recently gaining popularity due to rapid development of wireless technology used in the guidance, navigation and control.

Appendix

A. Lift due to Angle-of-Attack

$$L_\alpha^+(\psi,r) = \frac{1}{2}\rho|V_n|V_z C_{l\alpha+} C d\psi dr$$

$$= \frac{1}{2}\rho C\alpha C_{l\alpha+}|\mathrm{V}\cos\psi + r\omega|V d\psi dr$$

$$= \frac{1}{2}\rho V^2 C\alpha C_{l\alpha+}\left|\cos\psi + \left(\frac{r\chi}{R}\right)\right| d\psi dr$$

$$\overline{L_\alpha^+} = \frac{1}{2}\rho V^2 C\alpha C_{l\alpha+}\int_0^R \left\{\frac{1}{\pi}\int_0^{\pi-\cos^{-1}\left(\frac{r\chi}{R}\right)} \left[\cos\psi + \left(\frac{r\chi}{R}\right)\right] d\psi\right\} dr$$

$$= \frac{1}{2}\rho V^2 C\alpha C_{l\alpha+}\int_0^R \left\{\frac{r\chi}{R} + \frac{1}{\pi}\sqrt{1-\left(\frac{r\chi}{R}\right)^2} - \frac{1}{\pi}\left(\frac{r\chi}{R}\right)\cos^{-1}\left(\frac{r\chi}{R}\right)\right\} dr$$

$$= \frac{1}{2}\rho V^2 RC\alpha C_{l\alpha+}\left\{\frac{\chi}{2} + \frac{1}{2\pi}\left[\frac{3}{2}\sqrt{1-\chi^2} + \frac{\sin^{-1}\chi}{2\chi} - \chi\cos^{-1}\chi\right]\right\}$$

$$\overline{L_\alpha^-} = \frac{1}{2}\rho V^2 C\alpha C_{l\alpha-}\int_0^R \left\{\frac{1}{\pi}\int_{\pi-\cos^{-1}\left(\frac{r\chi}{R}\right)}^{\pi} \left[-\cos\psi - \left(\frac{r\chi}{R}\right)\right] d\psi\right\} dr$$

$$= \frac{1}{2}\rho V^2 C\alpha C_{l\alpha-}\int_0^R \left\{\frac{1}{\pi}\sqrt{1-\left(\frac{r\chi}{R}\right)^2} - \frac{1}{\pi}\left(\frac{r\chi}{R}\right)\cos^{-1}\left(\frac{r\chi}{R}\right)\right\} dr$$

$$= \frac{1}{2}\rho V^2 RC\alpha C_{l\alpha-}\left\{\frac{1}{2\pi}\left[\frac{3}{2}\sqrt{1-\chi^2} + \frac{\sin^{-1}\chi}{2\chi} - \chi\cos^{-1}\chi\right]\right\}$$

$$\overline{L_\alpha} = \overline{L_\alpha^+} + \overline{L_\alpha^-}$$

$$= \frac{1}{2}\rho V^2 RC\alpha C_{l\alpha+}\left\{\frac{\chi}{2} + \frac{1}{2\pi}\left(1 + \frac{C_{l\alpha-}}{C_{l\alpha+}}\right)\left[\frac{3}{2}\sqrt{1-\chi^2} + \frac{\sin^{-1}\chi}{2\chi} - \chi\cos^{-1}\chi\right]\right\}$$

$$\approx \frac{1}{2}\rho V^2 RC\alpha C_{l\alpha+}\left\{\frac{\chi}{2} + \left(1 + \frac{C_{l\alpha-}}{C_{l\alpha+}}\right)\left[\frac{1}{\pi} - \frac{\chi}{4} + \frac{\chi^2}{6\pi} + \frac{\chi^4}{120\pi}\ldots\right]\right\}$$

B. Rolling-Moment Derivation

$$M_{X0}^{+}(\psi,r) = \frac{1}{2}\rho V_n^2 C_{l0+} C.\, r\cos\psi\, d\psi dr$$

$$= \frac{1}{2}\rho V^2 C C_{l0+}\left[\cos\psi + \left(\frac{r\chi}{R}\right)\right]^2 .\, r\cos\psi\, d\psi dr$$

$$\overline{M_{X0}^{+}} = \frac{1}{2}\rho V^2 C C_{l0+}\int_0^R \left\{\frac{1}{\pi}\int_0^{\pi-\cos^{-1}\left(\frac{r\chi}{R}\right)} \left[\cos\psi + \left(\frac{r\chi}{R}\right)\right]^2 .\, r\cos\psi\, d\psi\right\} dr$$

$$= \frac{1}{2}\rho V^2 C C_{l0+}\int_0^R \frac{1}{3\pi}\left\{\left(2r + \frac{\chi^2 r^3}{R^2}\right)\sqrt{1-\left(\frac{r\chi}{R}\right)^2} + 3\chi\left(\frac{r^2}{R}\right)\left[\pi - \cos^{-1}\left(\frac{r\chi}{R}\right)\right]\right\} dr$$

$$= \frac{1}{6}\rho V^2 R^2 C C_{l0+}\chi\left\{1 + \frac{1}{15\pi\chi^3}\left[2 + (3\chi^4 - \chi^2 - 2)\sqrt{1-\chi^2}\right] + \frac{2}{3\pi\chi^3}\left[1 - (1-\chi^2)^{3/2}\right]\right.$$

$$\left. - \frac{1}{\pi}\left[\cos^{-1}\chi - \frac{1}{3\chi^3}\left[(2+\chi^2)\sqrt{1-\chi^2} - 2\right]\right]\right\}$$

$$\overline{M_{X0}^{-}} = \frac{1}{2}\rho V^2 C C_{l0-}\int_0^R \left\{\frac{1}{\pi}\int_{\pi-\cos^{-1}\left(\frac{r\chi}{R}\right)}^{\pi} \left[\cos\psi + \left(\frac{r\chi}{R}\right)\right]^2 .\, r\cos\psi\, d\psi\right\} dr$$

$$= \frac{1}{2}\rho V^2 C C_{l0-}\int_0^R \frac{1}{3\pi}\left\{-\left(2r + \frac{\chi^2 r^3}{R^2}\right)\sqrt{1-\left(\frac{r\chi}{R}\right)^2} - 3\chi\left(\frac{r^2}{R}\right)\left[-\cos^{-1}\left(\frac{r\chi}{R}\right)\right]\right\} dr$$

$$= \frac{1}{6}\rho V^2 R^2 C C_{l0-}\chi\left\{-\frac{1}{15\pi\chi^3}\left[2 + (3\chi^4 - \chi^2 - 2)\sqrt{1-\chi^2}\right] - \frac{2}{3\pi\chi^3}\left[1 - (1-\chi^2)^{\frac{3}{2}}\right]\right.$$

$$\left. + \frac{1}{\pi}\left[\cos^{-1}\chi - \frac{1}{3\chi^3}\left[(2+\chi^2)\sqrt{1-\chi^2} - 2\right]\right]\right\}$$

$$\overline{M_{X0}} = \overline{M_{X0}^{+}} + \overline{M_{X0}^{-}}$$

$$= \frac{1}{6}\rho V^2 R^2 C C_{l0+}\left\{\chi\right.$$

$$+ \left(1 - \frac{C_{l0-}}{C_{l0+}}\right)\left[\frac{1}{15\pi\chi^2}\left[2 + (3\chi^4 - \chi^2 - 2)\sqrt{1-\chi^2}\right] + \frac{2}{3\pi\chi^2}\left[1 - (1-\chi^2)^{3/2}\right]\right.$$

$$\left.\left. - \frac{1}{\pi}\left[\chi\cos^{-1}\chi - \frac{1}{3\chi^2}\left[(2+\chi^2)\sqrt{1-\chi^2} - 2\right]\right]\right\}$$

$$\approx \frac{1}{2}\rho V^2 R^2 C C_{l0+}\left\{\frac{\chi}{3}+\frac{1}{3}\left(1-\frac{C_{l0-}}{C_{l0+}}\right)\left[\frac{1}{\pi}-\frac{\chi}{2}+\left(\frac{3}{4\pi}\right)\chi^2-\left(\frac{1}{24\pi}\right)\chi^4 \dots\right]\right\}$$

$$M_{X\alpha}^{+}(\psi,r) = \frac{1}{2}\rho|V_n|V_z C_{l\alpha+} C r\cos\psi\, d\psi dr$$

$$= \frac{1}{2}\rho V^2 C\alpha C_{l\alpha+}\left|\cos\psi+\left(\frac{r\chi}{R}\right)\right| r\cos\psi\, d\psi dr$$

$$\overline{M_{X\alpha}^{+}} = \frac{1}{2}\rho V^2 C\alpha C_{l\alpha+}\int_0^R\left\{\frac{1}{\pi}\int_0^{\pi-\cos^{-1}\left(\frac{r\chi}{R}\right)}\left[\cos\psi+\left(\frac{r\chi}{R}\right)\right].r\cos\psi\, d\psi\right\}dr$$

$$= \frac{1}{2}\rho V^2 C\alpha C_{l\alpha+}\int_0^R\frac{1}{2\pi}\left\{\pi r+\frac{r^2\chi}{R}\sqrt{1-\left(\frac{r\chi}{R}\right)^2}-r\cos^{-1}\left(\frac{r\chi}{R}\right)\right\}dr$$

$$= \frac{1}{2}\rho V^2 R^2 C\alpha C_{l\alpha+}\left\{\frac{1}{4}+\frac{1}{16\pi\chi}\left[(2\square^2-1)\sqrt{1-\square^2}+\frac{\sin^{-1}\chi}{\square}\right]\right.$$

$$\left.-\frac{1}{8\pi\chi}\left[\frac{\sin^{-1}\chi}{\chi}+2\chi\cos^{-1}\chi-\sqrt{1-\chi^2}\right]\right\}$$

$$\overline{M_{X\alpha}^{-}} = \frac{1}{2}\rho V^2 C\alpha C_{l\alpha-}\int_0^R\left\{\frac{1}{\pi}\int_{\pi-\cos^{-1}\left(\frac{r\chi}{R}\right)}^{\pi}\left[-\cos\psi-\left(\frac{r\chi}{R}\right)\right].r\cos\psi\, d\psi\right\}dr$$

$$= \frac{1}{2}\rho V^2 C\alpha C_{l\alpha-}\int_0^R\frac{1}{2\pi}\left\{\frac{r^2\chi}{R}\sqrt{1-\left(\frac{r\chi}{R}\right)^2}-r\cos^{-1}\left(\frac{r\chi}{R}\right)\right\}dr$$

$$= \frac{1}{2}\rho V^2 R^2 C\alpha C_{l\alpha-}\left\{\frac{1}{16\pi\chi}\left[(2\chi^2-1)\sqrt{1-\chi^2}+\frac{\sin^{-1}\chi}{\chi}\right]-\frac{1}{8\pi\chi}\left[\frac{\sin^{-1}\chi}{\chi}+2\chi\cos^{-1}\chi-\sqrt{1-\chi^2}\right]\right\}$$

$$\overline{M_{X\alpha}} = \overline{M_{X\alpha}^{+}}+\overline{M_{X\alpha}^{-}}$$

$$= \frac{1}{2}\rho V^2 R^2 C\alpha C_{l\alpha+}\left\{\frac{1}{4}\right.$$

$$+\left(1+\frac{C_{l\alpha-}}{C_{l\alpha+}}\right)\left[\frac{1}{16\pi\chi}\left[(2\square^2-1)\sqrt{1-\square^2}+\sin^{-1}\chi\right]\right.$$

$$\left.\left.-\frac{1}{8\pi\chi}\left[\frac{\sin^{-1}\chi}{\chi}+2\chi\cos^{-1}\chi-\sqrt{1-\chi^2}\right]\right]\right\}$$

$$\approx \frac{1}{2}\rho V^2 R^2 C\alpha C_{l\alpha+}\left\{\frac{1}{4}-\left(1+\frac{C_{l\alpha-}}{C_{l\alpha+}}\right)\left[\frac{1}{8}-\frac{\chi}{3\pi}+\frac{\chi^3}{30\pi}+\frac{\chi^5}{280\pi}\dots\right]\right\}$$

C. Pitching-Moment Derivation

$$M_{Y0}^{+}(\psi,r) = \frac{1}{2}\rho V_n^2 C_{l0+} C.\, R_{offset}.\cos\psi\, d\psi dr$$

$$= \frac{1}{2}\rho V^2 C C_{l0+} R_{offset}\left[\cos\psi + \left(\frac{r\chi}{R}\right)\right]^2 \cos\psi\, d\psi dr$$

$$\overline{M_{Y0}^{+}} = \frac{1}{2}\rho V^2 C C_{l0+} R_{offset}\int_0^R \left\{\frac{1}{\pi}\int_0^{\pi-\cos^{-1}\left(\frac{r\chi}{R}\right)} \left[\cos\psi + \left(\frac{r\chi}{R}\right)\right]^2 \cos\psi\, d\psi\right\} dr$$

$$= \frac{1}{2}\rho V^2 C C_{l0+} R_{offset}\int_0^R \frac{1}{3\pi}\left\{3\pi\left(\frac{r\chi}{R}\right) + \left[2+\left(\frac{r\chi}{R}\right)^2\right]\sqrt{1-\left(\frac{r\chi}{R}\right)^2} - 3\left(\frac{r\chi}{R}\right)\cos^{-1}\left(\frac{r\chi}{R}\right)\right\} dr$$

$$= \frac{1}{2}\rho V^2 R C C_{l0+} R_{offset}\left\{\frac{\chi}{2} + \frac{1}{3\pi}\left[\sqrt{1-\chi^2} + \frac{\sin^{-1}\chi}{\chi}\right] + \frac{1}{24\pi}\left[(2\chi^2-1)\sqrt{1-\chi^2} + \frac{\sin^{-1}\chi}{\chi}\right]\right.$$
$$\left. - \frac{1}{4\pi}\left[\frac{\sin^{-1}\chi}{\chi} + 2\chi\cos^{-1}\chi - \sqrt{1-\chi^2}\right]\right\}$$

$$\overline{M_{Y0}^{-}} = \frac{1}{2}\rho V^2 C C_{l0-}\left(-R_{offset}\right)\int_0^R \left\{\frac{1}{\pi}\int_{\pi-\cos^{-1}\left(\frac{r\chi}{R}\right)}^{\pi} \left[\cos\psi + \left(\frac{r\chi}{R}\right)\right]^2 \cos\psi\, d\psi\right\} dr$$

$$= -\frac{1}{2}\rho V^2 C C_{l0-} R_{offset}\int_0^R \frac{1}{3\pi}\left\{\left[2+\left(\frac{r\chi}{R}\right)^2\right]\sqrt{1-\left(\frac{r\chi}{R}\right)^2} - 3\left(\frac{r\chi}{R}\right)\cos^{-1}\left(\frac{r\chi}{R}\right)\right\} dr$$

$$= -\frac{1}{2}\rho V^2 R C C_{l0-} R_{offset}\left\{-\frac{1}{3\pi}\left[\sqrt{1-\chi^2} + \frac{\sin^{-1}\chi}{\chi}\right] - \frac{1}{24\pi}\left[(2\chi^2-1)\sqrt{1-\chi^2} + \frac{\sin^{-1}\chi}{\chi}\right]\right.$$
$$\left. + \frac{1}{4\pi}\left[\frac{\sin^{-1}\chi}{\chi} + 2\chi\cos^{-1}\chi - \sqrt{1-\chi^2}\right]\right\}$$

$$\overline{M_{Y0}} = \overline{M_{Y0}^{+}} + \overline{M_{Y0}^{-}}$$

$$= \frac{1}{2}\rho V^2 R C C_{l0+} R_{offset}\left\{\frac{}{2}\right.$$
$$+ \left(1 + \frac{C_{l0-}}{C_{l0+}}\right)\left[\frac{1}{3\pi}\left[\sqrt{1-\chi^2} + \frac{\sin^{-1}\chi}{\chi}\right] + \frac{1}{24\pi}\left[(2\chi^2-1)\sqrt{1-\chi^2} + \frac{\sin^{-1}\chi}{\chi}\right]\right.$$
$$\left.\left. - \frac{1}{4\pi}\left[\frac{\sin^{-1}\chi}{\chi} + 2\chi\cos^{-1}\chi - \sqrt{1-\chi^2}\right]\right]\right\}$$

$$\approx \frac{1}{2}\rho V^2 RCC_{l0+}R_{offset}\left\{\frac{\chi}{2}+\left(1+\frac{C_{l0-}}{C_{l0+}}\right)\left[\frac{2}{3\pi}-\frac{\chi}{4}+\frac{\chi^2}{3\pi}-\frac{\chi^4}{60\pi}\dots\right]\right\}$$

$$M_{Y\alpha}^{+}(\psi,r)=\frac{1}{2}\rho|V_n|V_z C_{l\alpha+}CR_{offset}\cos\psi\, d\psi dr$$

$$=\frac{1}{2}\rho V^2 C\alpha C_{l\alpha+}R_{offset}\left|\cos\psi+\left(\frac{r\chi}{R}\right)\right|\cos\psi\, d\psi dr$$

$$\overline{M_{Y\alpha}^{+}}=\frac{1}{2}\rho V^2 C\alpha C_{l\alpha+}R_{offset}\int_0^R\left\{\frac{1}{\pi}\int_0^{\pi-\cos^{-1}\left(\frac{r\chi}{R}\right)}\left[\cos\psi+\left(\frac{r\chi}{R}\right)\right]\cos\psi\, d\psi\right\}dr$$

$$=\frac{1}{2}\rho V^2 C\alpha C_{l\alpha+}R_{offset}\int_0^R\left\{\frac{1}{2}+\frac{1}{2\pi}\left[\left(\frac{r\chi}{R}\right)\sqrt{1-\left(\frac{r\chi}{R}\right)^2}-\cos^{-1}\left(\frac{r\chi}{R}\right)\right]\right\}dr$$

$$=\frac{1}{2}\rho V^2 RC\alpha C_{l\alpha+}R_{offset}\left\{\frac{1}{2}+\frac{1}{6\pi\chi}\left[1-(1-\chi^2)^{3/2}\right]-\frac{1}{2\pi\chi}\left[1+\chi\cos^{-1}\chi-\sqrt{1-\chi^2}\right]\right\}$$

$$\overline{M_{Y\alpha}^{-}}=\frac{1}{2}\rho V^2 C\alpha C_{l\alpha-}\left(-R_{offset}\right)\int_0^R\left\{\frac{1}{\pi}\int_{\pi-\cos^{-1}\left(\frac{r\chi}{R}\right)}^{\pi}\left[-\cos\psi-\left(\frac{r\chi}{R}\right)\right]\cos\psi\, d\psi\right\}dr$$

$$=-\frac{1}{2}\rho V^2 C\alpha C_{l\alpha-}R_{offset}\int_0^R\left\{\frac{1}{2\pi}\left[\left(\frac{r\chi}{R}\right)\sqrt{1-\left(\frac{r\chi}{R}\right)^2}-\cos^{-1}\left(\frac{r\chi}{R}\right)\right]\right\}dr$$

$$=-\frac{1}{2}\rho V^2 RC\alpha C_{l\alpha-}R_{offset}\left\{\frac{1}{6\pi\chi}\left[1-(1-\chi^2)^{\frac{3}{2}}\right]-\frac{1}{2\pi\chi}\left[1+\chi\cos^{-1}\chi-\sqrt{1-\chi^2}\right]\right\}$$

$$\overline{M_{Y\alpha}}=\overline{M_{Y\alpha}^{+}}+\overline{M_{Y\alpha}^{-}}$$

$$=\frac{1}{2}\rho V^2 RC\alpha C_{l\alpha+}R_{offset}\left\{\frac{1}{2}+\left(1-\frac{C_{l\alpha-}}{C_{l\alpha+}}\right)\left[\frac{1}{6\pi\chi}\left[1-(1-\chi^2)^{3/2}\right]-\frac{1}{2\pi\chi}\left[1+\chi\cos^{-1}\chi-\sqrt{1-\chi^2}\right]\right]\right\}$$

$$\approx \frac{1}{2}\rho V^2 RC\alpha C_{l\alpha+}R_{offset}\left\{\frac{1}{2}-\left(1-\frac{C_{l\alpha-}}{C_{l\alpha+}}\right)\left[\frac{1}{4}-\frac{\chi}{2\pi}+\frac{\chi^3}{24\pi}+\frac{\chi^5}{240\pi}\dots\right]\right\}$$

Acknowledgments

The authors would like to thank the International Federation of Boomerang Associations (IFBA) and the many athletes of the 2018 World Boomerang Championship (WBC) who willingly and enthusiastically shared their knowledge of designing and throwing boomerangs. Gary Broadbent deserves special thanks for sharing his extensive experience in the construction of the boomerangs and its impact on the flight trajectory. Thanks to Dana Larrabee for introducing the first author to the amazing world of boomerangs. Also, thanks to Prof. Mark Anderson in the Mechanical and Aerospace Engineering for his valuable time and patience in teaching the basics of Aerodynamics.

References

[1] "International Federation of Boomerang Associations Official Rule Book: Team and Individual Events," 2018.

[2] John Cross, "Performance Boomerangs," 2012. 2nd edition.

[3] https://en.wikipedia.org/wiki/Boomerang.

[4] J. Mauro, "An Introduction to Boomerangs," Smith & Flannery, Inc., 1989, 3rd Edition.

[5] Michael Siems, "New Ultimate Boomerang Book," 2012.

[6] F. Hess, "Boomerangs, Aerodynamics and Motion," Ph.D. Thesis, Groningen University, June 1975.

[7] Akira Azuma, Goro Beppu, Hiroaki Ishikawa, and Kunio Yasuda, "Flight Dynamics of the Boomerang, Part 1: Fundamental Analysis," Journal of Guidance, Control, and Dynamics, Vol. 27, No. 4, 2004, pp. 545-554.

[8] Goro Beppu, Hiroaki Ishikawa, Akira Azuma, and Kunio Yasuda, "Flight Dynamics of the Boomerang, Part 2: Effects of Initial Condition and Geometrical Configuration," Journal of Guidance, Control, and Dynamics, Vol. 27, No. 4, 2004, pp. 555-563.

[9] John Vassberg, "Boomerang Flight Dynamics," 30th AIAA Applied Aerodynamics Conference, 2012.

[10] XFOIL Subsonic Airfoil Development System.

[11] Daniele Ragni, Carlos Sim~ao Ferreira and Matthew Barone "Experimental and numerical investigation of an optimized airfoil for vertical axis wind turbines," 32nd ASME Wind Energy Symposium, 2015

[12] Weisheng Chen and Luis P. Bernal "Design and Performance of Low Reynolds Number Airfoils for Solar-Powered Flight," 46th AIAA Aerospace Sciences Meeting and Exhibit, 2008.

Biography

Prasad S. Gudem received the B. Tech degree in Electrical Engineering from the Indian Institute of Technology, Madras, India, in 1988, and the Ph.D. degree in Electrical Engineering from the University of Waterloo, Waterloo, Ontario, Canada, in 1996. He was a Vice President of Engineering at Qualcomm from 2014-2018 and currently an Adjunct faculty in the Department of Electrical and Computer Engineering, University of California at San Diego, La Jolla, CA, USA. He has 50+ patents and 40+ IEEE publications. He taught several graduate-level classes and co-advised twelve Ph.D. students in RF integrated circuit (IC) design. Dr. Gudem was the recipient of the Graduate Teaching Award in recognition of his outstanding teaching of the ECE265 course sequence, "Communication Circuit Design: I, II, and III". He is an avid follower of the history of STEM (Science, Technology, Engineering, and Mathematics).

Manuel Schütz received his degree (lic.phil.nat) in physics from the Institute of Applied Physics, University of Bern, Bern, Switzerland in 2003. He is a five-time World Champion in boomerang throwing and holds several world records, among them the long-distance world record (apex at 238m). Since 2009, he is a mathematics and science teacher at WKS KV Bildung in Bern (Federal Vocational Baccalaureate).

Kyle Holland received a Ph.D degree in electrical engineering from the University of Alberta, Edmonton, AB, Canada in 2016. He is currently a senior engineer in the RFIC Design Group with Qualcomm Technologies, Inc., San Diego, CA, USA. His research interests include the quantum-mechanical simulations of nano-electronic devices, N-Path filters, and future electronics.